**Comparative analysis of rhesus macaque and human placental organoids highlights evolutionary differences in placentation**

Allyson Caldwell[1], Liheng Yang[1], Elizabeth A. Scheef[2], Amitinder Kaur[2], Carolyn B. Coyne*[1,3]

1 Duke University School of Medicine, Department of Integrative Immunobiology, Durham, NC
2) Tulane National Primate Research Center, Tulane School of Medicine, Covington, LA, 70433, USA.
3) Duke Human Vaccine Institute, Durham, NC

*Address correspondence:
Carolyn Coyne, PhD
3130 Medical Sciences Research Building III
3 Genome Court
Durham, NC 27710
USA
carolyn.coyne@duke.edu

**Abstract**

Throughout evolution, the placenta has diversified in both structure and cellular composition while maintaining its fundamental function. Trophoblasts are fetal-derived cells responsible for nourishing and protecting the developing fetus and are a universal component of all placentas. While primate placentas exhibit many shared morphological features, species-specific differences in gene expression remain largely unexplored, primarily due to the lack of suitable *in vitro* models. To address this gap, we developed organoids from rhesus macaque placentas, including trophoblast and maternal-derived decidua types, and compared them with organoids derived from human placentas. We performed comparative single-cell RNA sequencing to delineate shared and distinct transcriptional signatures between rhesus macaque and human trophoblasts. We further defined the differentiation trajectories leading to the multinucleated syncytiotrophoblast, highlighting both shared and unique transcriptional signatures between rhesus macaque and human placentas. This work establishes novel *in vitro* models of the non-human primate placenta and characterizes distinct trophoblast gene profiles in rhesus macaques and humans, providing insights into interspecies variations in placental biology.

## Introduction

The placenta lies at the maternal-fetal interface during pregnancy, and both nourishes and protects the developing fetus. Hemochorial placentas are characterized by direct contact between fetal cells and maternal blood. Trophoblasts are fetal-derived cells that are essential for proper formation and function of the placenta. In hemochorial mammals like humans and rhesus macaques, a trophoblast layer called the chorion fuses with the allantois, an extra-embryonic membrane that forms from the embryo's hindgut, to develop a chorioallantoic placenta. As the chorioallantoic placenta has evolved, trophoblasts have been conserved over time[1] and now include a variety of trophoblast populations. In hemochorial mammals, these populations include cytotrophoblasts (CTBs) that can differentiate into other trophoblast subtypes including extravillous trophoblasts (EVTs) and the syncytiotrophoblast (STB). EVTs are located at the villous columns and invade into the decidualized endometrium where the placenta is attached during pregnancy. In early stages of gestation, EVTs remodel the maternal microvasculature to facilitate the entry of maternal blood into the intervillous space. The STB is the multinucleated trophoblast monolayer covering the surface of the hemochorial placenta and is formed by the fusion of mononuclear CTBs. The cellular heterogeneity and complexity of the placenta presents a major challenge to accurately recapitulate placental biology *in vitro*, especially across species.

Rhesus macaques and humans develop morphologically similar placentas that contain comparable cell layers [2]. These similarities, along with the close evolutionary relationship between rhesus macaques and humans, make rhesus macaques an excellent research model to study human placentation and pregnancy. However, despite their similarities, previous studies have identified key differences in the transcriptional signatures between rhesus macaque and human trophoblasts[3]. For example, while human trophoblast populations express markers including HLA-G, SIGLEC-6, and ERVW-1, these markers are absent in the rhesus macaque placenta[4-7]. However, these previous comparative studies were performed using whole placental tissue rather than in distinct trophoblast cell populations.

53 Organoids are three-dimensional models that often contain the cellular heterogeneity
54 existing within their tissue of origin. Human trophoblast organoids have been validated as a model
55 that accurately recapitulates the cellular heterogeneity within the human placenta and can be
56 propagated and cryopreserved[8-10]. Our laboratory has previously developed human trophoblast
57 organoids (hTO) and decidua organoids (hDO) from full-term placental tissue[10]. These organoids
58 release pregnancy-associated hormones, differentiate to contain key trophoblast subpopulations
59 present in the human placenta, and accurately recapitulate the transcriptional profile of
60 trophoblasts observed *in vivo*[10,11]. Moreover, despite their isolation from full-term tissue, hTOs
61 more closely resemble trophoblasts in first-trimester tissue[10,11]. These qualities make placental
62 organoids a more physiologically relevant model than other *in vitro* models, such as cell lines
63 derived from choriocarcinomas. In addition to tissue-derived organoids, trophoblast stem cells
64 (TSC) have been developed as an *in vitro* model of both the human and rhesus macaque
65 placentas[12,13]. TSC models consist of proliferative mononuclear cytotrophoblasts that do not
66 spontaneously differentiate into trophoblast lineages but instead require exogenous agents (e.g.,
67 forskolin) to induce differentiation. While recapitulating aspects of trophoblast biology, there are
68 key differences between tissue-derived TOs and TSCs, with TSC-derived models lacking key
69 transcriptional signatures associated with trophoblast lineages[11,14].

70 Here, we developed rhesus macaque trophoblast organoids (rTO) and decidua organoids
71 (rDO) from matched late gestation placentas. Morphologically, rTOs and rDOs closely resembled
72 organoids derived from human tissue and expressed canonical markers of placental tissue.
73 Moreover, these organoids recapitulated the hormone release and transcriptional signature of
74 rhesus macaque placental tissue. To characterize the cellular heterogeneity of rTOs, we
75 performed single-cell RNA sequencing (scRNA-seq) and conducted comparative analyses with
76 hTOs. Using this approach, we defined the transcriptional signatures of distinct rhesus macaque
77 trophoblast populations and identified shared and unique gene signatures in human trophoblasts.
78 Lastly, we compared the differentiation trajectory from CTBs to the STB between rTOs and hTOs

and identified species-specific genes associated with STB formation. Altogether, this work establishes new *in vitro* models of the rhesus macaque placenta, allowing for direct cross-species comparisons to model human and non-human primate placentation.

## Results

### Derivation of trophoblast and decidua organoids from rhesus macaque placentas

To generate matched trophoblast and decidua organoids, we dissected fetal and maternal tissues from mid-late third trimester gestation rhesus macaque placentas (143-154 gestational days) (**Figure 1A**). The architecture of chorionic villi is similar between rhesus macaque and human placentas, but rhesus macaques exhibit shorter, wider, and less branched villi than do humans (**Figure 1B**). To develop rhesus macaque trophoblast organoids (rTOs), we dissected the chorionic villi and smooth chorion and carefully removed any decidua tissue. The chorionic villi and smooth chorion were homogenized using similar protocols that were developed previously to isolate human trophoblast organoids (hTOs) from full-term placental tissue[10]. To develop decidua organoids (rDOs), we isolated progenitor cells from decidual glands, following a similar approach as described for human DOs (hDOs). Isolated progenitor cells from the fetal and maternal tissues were then cultured to develop rhesus macaque placental organoids in previously defined term trophoblast organoid media (TOM) used for hTOs**.** Organoids were visible ~5-7 days post-isolation and were passaged every ~7-10 days (rTOs) or every ~5-7 days (rDOs) once established. Morphologically, rTOs and rDOs resembled hTOs and hDOs (**Figure 1C**) and could be propagated long-term (>15 passages) without loss of this morphology (**Figure 1D**). Confocal microscopy for cytokeratin-19 confirmed the architecture of rhesus macaque organoids, which were similar to those derived from human placental tissue **(Figure S1A-B)**. Collectively, these data demonstrate the successful derivation of rTOs and rDOs from rhesus macaque placental tissue.

105 **Rhesus macaque-derived placenta organoids secrete pregnancy hormones and express**
106 **canonical markers**

107 To examine the localization of canonical trophoblast and decidua markers in rTOs and rDOs, we
108 performed immunostaining using cell-type specific markers. In rTOs, this included the STB marker
109 Syndecan-1 (SDC-1) and the CTB marker integrin alpha-6 (ITGA6). rTOs and hTOs both
110 expressed SDC-1, indicating the presence of the fused STB and ITGA6 representing the
111 mononuclear CTBs **(Figure 1E and 1F).** Unlike hTOs, which develop with an inward facing STB,
112 SDC-1 localization suggested that rTOs developed with an outward facing STB **(Figure 1E and**
113 **1F**, **Supplemental Movies 1 and 2)**. Additionally, rDOs expressed decidua gland-associated
114 markers including E-cadherin and the mucin MUC5AC, similar to their expression in hTOs **(Figure**
115 **1G and 1H)**.

116 Human TOs secrete essential pregnancy hormones including human chorionic
117 gonadotropin (hCG)[8,10]. During pregnancy, the rhesus macaque placenta secretes chorionic
118 gonadotropin (mCG) early in pregnancy with a peak occurring at approximately gestation day 22-
119 24[15]. In addition, progesterone is secreted during rhesus macaque pregnancy similar to human
120 pregnancy, with fluctuations throughout gestation[15]. Therefore, we investigated whether rTOs
121 secreted mCG and/or progesterone. To do this, we used two approaches including unbiased mass
122 spectrometry of conditioned medium (CM) collected from rTOs and an established
123 radioimmunoassay[16,17]. For mass spectrometry, we collected CM from three independent wells of
124 rTOs derived from two unique placentas and isolated bands migrating at ~26kD and ~10kD, the
125 approximate size of chorionic gonadotropin A (CGA), on a reducing SDS-PAGE gel (**Figure S1C**).
126 Spectral counts for CGA, which is secreted with CG beta subunits to form mCG, were detected
127 in every conditioned media (CM) sample isolated from rhesus trophoblast organoids (rTOs), with
128 high identification probability (**Figure 1I, 1J**). In contrast, no spectral counts for CGA mapped in
129 any non-conditioned medium (NCM) control samples (**Figure 1I, 1J**). To directly quantify the
130 levels of mCG and progesterone secreted from rTOs, we collected CM from three unique rTOs

131 lines and performed a radioimmunoassay described previously[16,17]. NCM controls were assayed
132 in triplicate and subtracted from rTO conditioned media samples. We found high levels of mCG
133 (>1000ng/mL) and progesterone (>1200ng/mL) in rTO conditioned media, **(Figure 1K)**. Similar to
134 hTOs, rTOs can be passaged long-term without loss of mCG or progesterone secretion.

135 Lastly, we performed bulk RNA sequencing of rTOs and rDOs to assess the expression of
136 known canonical markers of human trophoblasts or glandular epithelial cells, respectively, and to
137 verify the absence of contamination of other tissues/cells[10,13]. To do this, we compared the
138 expression profile of canonical markers of rhesus-derived trophoblasts or decidua epithelial
139 organoids. We found that rTOs highly expressed trophoblast-specific markers, including PGF,
140 MMP2, and ITGA5 which were absent or expressed at low levels in rDOs **(Figure S1D)**. We also
141 found that that rTOs expressed markers of distinct trophoblast lineages including the STB (e.g.,
142 CGA), CTBs (e.g., FOXO4), and EVTs (e.g., MAMU-AG). Conversely, rDOs expressed markers
143 associated with the maternal decidua including MUC1, MUC20, and SOX17, which were absent
144 or expressed at low levels in rTOs **(Figure S1D)**. These results were similar to the differences
145 observed between hTOs and hDOs **(Figure S1E)**.

146 We next analyzed the transcriptional dataset to identify non-annotated genes associated
147 with rhesus macaque trophoblasts, which included pregnancy-specific glycoproteins (PSGs).
148 PSGs have been described in many non-human species, including primates, mice, horses, and
149 cows[18]; however, the driving forces of evolution of these genes is unclear. Rhesus macaque PSGs
150 have not been annotated with gene names in the recent *Macaca Mulatta* genome assembly,
151 *Mmul10*. We identified rhesus macaque PSGs in the rTO dataset by comparing the genome
152 sequence of unannotated macaque genes to the human genome (hg38) using BLAST. We
153 identified five PSGs that were also expressed in rTOs **(Figure S1F)**. There are ten identified PSGs
154 in the human genome that are expressed in hTOs **(Figure S1G)**. Together, these data show that
155 rTOs and rDOs recapitulate the transcriptional profile of the rhesus macaque placenta and
156 express cell type-associated markers.

157

158 **Single-cell RNA-seq mapping of rTOs reveals comparable cellular heterogeneity to hTOs**

159 Human TOs self-differentiate to contain many of the major trophoblast cell types present in the
160 human placenta. To determine if rTOs recapitulate trophoblast heterogeneity observed *in vivo*, we
161 performed single-cell RNA sequencing (scRNA-seq). In parallel, we performed scRNA-seq from
162 hTOs to directly compare trophoblast populations between rTOs and hTOs. Established lines of
163 rTOs and hTOs were dissociated into single cell suspensions and processed separately to identify
164 cell types present in TOs. A total of 11,916 (rTOs) and 15,766 (hTOs) cells passed quality control
165 and were used for cluster analysis and cell-type specific marker expression analysis following
166 integration to correct for batch effects. Clustering analysis revealed five major cell populations
167 present in both rTOs and hTOs (**Figure 2A**, **2B**) which were distributed similarly across all TO
168 lines (**Figure 2C, 2D, S2A**). To define the specific cellular identity of these clusters, we identified
169 gene enrichment profiles of each cluster and mapped these transcriptional signatures to canonical
170 trophoblast markers[3,13]. Clusters in rTOs included two non-proliferative CTB populations (CTB-1
171 and -2) which accounted for ~31% and ~20% of all populations respectively, two proliferating CTB
172 populations (CTBp-1 and -2) which accounted for ~24% and ~23%, and one STB population
173 which only accounted for 2% (**Figure 2A, 2C**). Given the multinucleated nature of the STB, it is
174 less represented in scRNA-seq datasets from both tissue and TOs[11]. CTB clusters were enriched
175 in canonical markers including KRT7 and CDH1 whereas CTB-p clusters were enriched in genes
176 associated with proliferation (e.g., MKI67, CCNA2) (**Figure 2E, 2G**). One population of CTBs,
177 CTB-2, was enriched in markers of EVTs including NOTCH2 and NCAM1 but was lacking the fully
178 differentiated EVT marker MAMU-AG (**Figure 2E**). The STB population was enriched in canonical
179 markers including TFAP2A, INSL4, HOPX, CGA, and the endogenous retrovirus fusion gene
180 ERVFRD-1 (**Figure 2E, 2G**). Many genes previously identified in TSC-derived rhesus macaque
181 lineages to be expressed in CTBs (**Figure S2C**) and STB/EVTs (**Figure S2D**) were also
182 expressed in a lineage-specific manner[13]. Unbiased cluster gene enrichment analysis also

183 demonstrated that as expected, both CTBp clusters were enriched for genes associated with cell
184 division (e.g., CENPF, CCNB1) and histones (e.g., H1-5, H1-3) (**Figure S2E**). In contrast, the
185 CTB-1 cluster in rTOs was enriched in gene associated with extracellular matrix (e.g., LAMB3,
186 LAMC2) and the regulation of MMPs (e.g., TIMP1, TIMP3) whereas CTB-2 was enriched in genes
187 associated with GTPases and GTP-binding proteins (e.g., ARL15, AGAP1) and NOTCH signaling
188 (e.g., MAML2, MAML3) (**Figure S2E**). These expression profiles were distinct from genes
189 enriched in the STB, which included canonical markers (e.g., HOPX, CGA) and several non-
190 annotated genes (e.g., ENSMMUG00000049714, ENSMMUG00000063643) (**Figure S2E**). Many
191 of the non-annotated STB-enriched genes are predicted to encode for rhesus macaque CGBs
192 (ENSMMUG00000040968, ENSMMUG00000063643, ENSMMUG00000049714) and PSGs as
193 we described above (ENSMMUG00000039210, ENSMMUG00000050799,
194 ENSMMUG00000047533) (**Figure S2F, S2G**). Previous studies described the expression of
195 CGBs in macaque trophoblast stem cell lines[13,19] but these studies did not state which specific
196 CGBs were present. The GO terms and genes associated with population-specific trophoblast-
197 enriched genes included the regulation of cell locomotion, motility, and migration, actin
198 cytoskeletal organization and processes (e.g., ACTG1, PFN1, CDC42) in CTB-1 whereas those
199 associated with CTB-2 were involved in the regulation of GTPase and hydrolase activities (e.g.,
200 RGL1, SNX13, RALGPS2, ARFGEF1) (**Figure S2H, S2I**). These pathways and genes were
201 distinct from the STB, in which pathways including protein catabolic processes and
202 endomembrane system organization were enriched (e.g., FOLRF1, EHD3, RAB11A) (**Figure
203 S2H, S2I**). STB-associated GO terms and associated genes included catabolic processes,
204 synaptic vesicle maturation, and protein localization to the plasma membrane (**Figure S2H, S2I**).
205 These data highlight the distinct cellular processes and functions amongst distinct rhesus
206 macaque trophoblast populations in rTOs.

207 Clusters in hTOs included two non-proliferative CTB populations (CTB-1 and -2) which
208 accounted for ~24% and ~15% of all populations respectively, two proliferating CTB populations

209 (CTBp-1 and -2) which accounted for ~27% and ~24%, and one STB population which only
210 accounted for 8% (**Figure 2B, 2D**). Gene enrichment in hTOs was similar to rTOs, with pCTBs
211 highly enriched for markers of proliferation (e.g., MKI67 and CCNA2), CTBs enriched for
212 canonical markers (e.g., KRT7 and CDH1), and STBs enriched for canonical marker (e.g.,
213 TFAP2A, INSL4, HOPX, ERVW-1, and CYP19A1) **(Figure 2F, 2H)**. Also like rTOs, one CTB
214 cluster, CTB-2, expressed markers of undifferentiated EVTs including ITGB1 and expressed low
215 levels of the canonical EVT marker HLA-G (**Figure 2F**). Collectively, these data define the cellular
216 composition of rhesus macaque- and human derived-trophoblast organoids and show that these
217 organoids differentiate into multiple trophoblast lineages.
218

219 **Pseudotime analysis reveals STB lineage markers in rTOs**

220 Trajectory analysis is a powerful tool for defining gene expression changes along the
221 differentiation of CTBs into the fused STB and can map dynamic gene expression to identify key
222 regulatory genes and pathways critical for STB formation. To define the STB differentiation
223 trajectory in rTOs and hTOs, we used the Slingshot algorithm for pseudotime gene expression
224 inference, establishing the global lineage structure with undefined starting and ending clusters[20].
225 We then depicted the pseudotime trajectory on the UMAP for the STB lineage in both rTOs
226 (**Figure 3A**) and hTOs (**Figure 3B**). In both cases, there was a continuous trajectory starting from
227 CTB-p populations, traversing through CTBs, and then culminating in the STB (**Figure 3A, 3B,**
228 **Table S6, S7**). Next, we conducted pseudotime expression analysis using tradeSeq in both rTOs
229 and hTOs. We observed an increase in canonical STB marker genes along the rTO STB
230 differentiation trajectory, including GCM1 and HOPX (**Figure 3C**). In hTOs, there was an increase
231 in STB marker genes such as HMOX1, INSL4, and CY19A1 (**Figure 3D**). Canonical markers,
232 including HOPX, showed increased expression along both the rTO and hTO trajectories (**Figures**
233 **3E and 3F**). In rTOs, other upregulated genes included the CGB homolog
234 ENSMMUG00000049714 and the endogenous retrovirus fusion gene ERVFRD-1 (**Figure 3G**),

while transcripts associated with replication (e.g., MKI67) and canonical markers of CTBs (e.g., CDH1) were downregulated (**Figure 3G**). Similar trajectories were observed in hTOs, where CGBs and ERVW-1 were upregulated along the STB trajectory, and MKI67 and CDH1 were downregulated (**Figure 3D and 3H**). These data define gene expression changes underlying the differentiation of rhesus macaque CTBs into STBs, offering insights into the molecular mechanisms driving placental development and evolution.

**Defining trophoblast marker divergence and convergence in rTOs and hTOs**

Next, we integrated scRNA-seq datasets from rTOs and hTOs to perform an evolutionary gene expression analysis, aiming to identify both divergence and convergence in cell marker expression between the two species. This analysis revealed five conserved clusters, most of which were comprised of near-equivalent ratios of rTO- and hTO-derived cells (**Figure 4A**, **4B**). These populations were conserved across independent rTO and hTO lines (**Figure S3A**). Clusters expressed canonical markers of CTB-p (e.g., MKI67, TOP2A), CTBs (e.g., CDH1, KRT7), and the STB (e.g., TFAP2A, HOPX) (**Figure 4C**). Expression of these canonical markers was conserved in both rTO and hTO datasets (**Figure 4D**). Unbiased gene enrichment analysis identified select genes defining two CTBp clusters (CTBp-1, CTBp-2), two CTB clusters (CTB-1, CTB-2) and a single STB cluster (**Figure S3B**). We did not observe a distinct EVT clusters in the combined dataset but select clusters did express both rhesus macaque and human EVT markers **(Figure S3C)**. Utilizing the clusterProfiler algorithm that allows for analysis and visualization functional profile of gene clusters[21], we performed gene ontology enrichment analysis on the rhesus macaque and human pathways and identified pathways associated with molecular functions that were enriched in the separate datasets (**Figure S3D-F)**.

We next focused on differential expression in the STB cluster between rTOs and hTOs, as this cell type is conserved across species; however, the extent to which its expression profile differs remains largely unknown. We found that there was near-equivalent expression of canonical

STB genes including HOPX, INSL4, CGA, amongst others, in both rTOs and hTOs (**Figure 4E**). We also observed the expression of orthologs in the STB cluster, including genes such as CGBs and PSGs that were expressed at similar levels in both rTOs and hTOs (**Figure 4F**). To elucidate differences in the transcriptional profiles of the STB markers rTOs and hTOs, we performed pseudobulk differential expression analysis using DeSEq2. This analysis identified differences in STB-associated transcriptional profiles and highlighted variations in gene expression arising from differences in annotation and/or gene presence between the human and rhesus genomes **(Figure 4G)**. Of the STB markers in the integrated dataset, 15.1% were shared between the two species **(Figure 4G)**. These markers included prostaglandin growth factor (CAPN6), inhibin subunit alpha ( INHA), and ERVFRD-1) (**Figure 4H**). rTO-specific STB markers accounted for 48.4% of the STB markers and 27.3% of these genes were found only in the rhesus macaque genome (**Figure 4G**). hTO-specific STB markers made up 36.6% of the STB markers and 25.9% of these markers were found only in the human genome (**Figure 4G**). We therefore focused on defining gene expression conservation and variance from genes conserved in both genomes. This analysis revealed significant differences in STB marker expression between rTOs and hTOs. For example, the STB in rTOs expressed the peptide hormone corticotropin-releasing hormone (CRH), the transcription factor ELF4, and the cytokeratin KRT81, amongst others (**Figure 4I, 4J**). In contrast, hTOs were enriched in genes including CYP19A1, the endogenous retrovirus gene ERVV-1, and the chemokine CCL5 (**Figure 4K, 4L**). These data illustrate that while there are shared markers within the STB populations of rTOs and hTOs, there are also species-specific markers in this specialized cell population.

**Pseudotime analysis uncovers species-specific gene trajectories in the STB lineage between rTOs and hTOs**

Given the significant differences in gene expression profile of STB population between rTOs and hTOs, we conducted a comparative Slingshot pseudotime trajectory analysis using the integrated

287 rTO and hTO dataset to infer gene expression along the CTBp to STB differentiation. This
288 pseudotime analysis revealed a continuous STB trajectory, progressing from proliferative CTB to
289 non-proliferating CTB and finally to the differentiated STB subtype (**Figure 5A**). STB
290 differentiation was characterized by increased expression of well-known STB markers INSL4,
291 PDLIM2, HMOX1, GCN1, and ERVFRD-1, which were upregulated in both rTOs and hTOs
292 **(Figure 5B, 5C, 5D, Table S8)**. Next, we compared species-specific gene trajectories between
293 rTOs and hTOs by analyzing the integrated dataset, separating the data by condition. This
294 analysis revealed species-associated differences in gene expression along the STB trajectory in
295 rTOs and hTOs. The rTO gene trajectory showed increased expression of PAGE4, SLC2A1,
296 WNT5A, and NGF in the STB trajectory, while these genes were unchanged or downregulated in
297 the hTO trajectory (**Figure 5E-5H**). Conversely, SDC3, TGFB1, HSPB1, and ESAM specifically
298 increased only in the hTO STB trajectory, with no similar increase in rTOs (**Figure 5I-5L**).
299 Altogether, these findings highlight species-specific differences in gene expression dynamics
300 along the STB differentiation trajectory.
301
302 **Cross-species signaling dynamics in hTOs and rTOs**
303 Trophoblasts are central to the autocrine and paracrine signaling networks that regulate placental
304 function and are crucial for maintaining a successful pregnancy. However, whether these
305 networks differ across species remains largely unknown. To define rhesus macaque and human
306 trophoblast signaling networks using TOs, we utilized the CellChat package in R[22]. This package
307 facilitates the inference of cell-cell interactions, helping to uncover communication pathways by
308 leveraging a comprehensive database of ligand-receptor pairs. To enhance this database, we
309 expanded it to include endogenous retrovirus-receptor interactions (ERVs), hormone signaling
310 pathways (e.g., hCG, CSH, PRL), and rhesus macaque-specific interactions (e.g., MAMU-E,
311 MAMU-AG). We used differential CellChat analysis to identify both shared and distinct signaling
312 pathways across species using the integrated rTO and hTO dataset. This analysis revealed a total

313 of 51 communication networks in rTOs and 36 networks in hTOs (**Figure S4A, S4B, Table S9,**
314 **S10**). These networks spanned both outgoing and incoming signals across all cell clusters
315 (**Figure 6A**). Next, we defined the patterns of this signaling, which identified the recurring
316 communication behaviors and networks between cell populations, revealing dominant signaling
317 pathways and highlighting how these pathways are shared or distinct across different populations.
318 This revealed four independent signaling patterns in rTOs, which included patterns associated
319 with individual clusters (Pattern 2-4), as well as patterns shared between clusters (Pattern 1)
320 (**Figure 6B**). Similarly, three patterns were identified in hTOs, which included those shared
321 amongst both CTBp and CTB populations (Pattern 1) and those specific to either CTB-2 or STB
322 (**Figure 6C**).

323 We analyzed the cell-type specificity of signaling pathways across distinct trophoblast
324 populations and between species. This revealed a high degree of autocrine and paracrine
325 signaling in all cell populations within both rTOs and hTOs (**Figure 6D**, **6E**). In rTOs, 33% of
326 networks were shared across clusters, with an additional 23% shared among all CTB populations
327 but absent in STB (**Figure S4C**). Similarly, in hTOs, 41% of pathways were shared across
328 populations, with 24% specific to CTB-derived clusters (**Figure S4D**). In both rTOs and hTOs, the
329 STB was most enriched in unique networks, which accounted for 10% and 5%, respectively, of
330 total networks (**Figure S4C, S4D**). CTB-associated networks included junction interactions (e.g.,
331 CDH and JAM) and NOTCH signaling, which were conserved between rTOs and hTOs (**Figure**
332 **6D, 6E**). The CTB-2 population in both rTOs and hTOs showed enrichment for specific pathways
333 compared to other CTB clusters, including WNT signaling in both rTOs and hTOs, endothelins
334 (EDNs) in rTOs, and OCLN in hTOs (**Figure 6D, 6E**). The STB population in both rTOs and hTOs
335 exhibited the most distinct signaling pathways, including CDH5 and ERVs in both species (**Figure**
336 **6D, 6E**). Additionally, some signaling pathways were enriched in different cell clusters in a
337 species-specific manner. For example, CCL signaling was active in both rTOs and hTOs, but the
338 responsible clusters differed: CTBp-1 in rTOs and STB in hTOs (**Figure 6D, 6E**).

339 Because we observed differences in trophoblast signaling between rTOs and hTOs, we
340 used comparative CellChat analysis to identify clusters and ligand-receptor pairs driving these
341 species-specific variations. Using this analysis, we found that although rTOs and hTOs contained
342 similar numbers of total signaling interactions, the strength of these interactions was significantly
343 higher in rTOs (**Figure S4E**). These differences were driven primarily by the CTB-2 cluster
344 (**Figure S4F**). Over 50% of pathways were conserved between rTOs and hTOs (**Figure S4G**),
345 with the highest conservation among CTB populations and the lowest in STB (**Figure S4H**).
346 Species-specific pathways, including those associated with IGF, EGF, and NCAM, were active
347 only in rTOs (**Figure 6F, Figure S4G**). We then identified ligand-receptor pairs linked to these
348 differences, focusing on the STB due to its significant species-related variations. Seven ligand-
349 receptor pairs were significantly downregulated in the STB of rTOs, particularly in PGF, ERVs,
350 and CCL signaling (**Figure 6G**). Differences in PGF and ERV signaling were mainly due to the
351 absence of key genes in rTOs, such as the receptor tyrosine kinase FLT1 and the endogenous
352 retrovirus fusion gene ERVW-1 (**Figure S4I**). In CCL signaling, while the STB of hTOs highly
353 expressed CCL5, this chemokine was absent in rTOs, where CCL signaling was instead driven
354 by CCL2 expression across CTB populations (**Figure 6H, S4I**). There were 21 signaling
355 upregulated ligand-receptor pairs in the STB of rTOs, the most significant of which was associated
356 with IGF signaling (**Figure 6I**). This enrichment was driven by the high expression of IGF2
357 throughout all clusters in rTOs, which was absent from hTOs (**Figure 6I, 6J, Figure S4J**). These
358 findings underscore the shared and distinct signaling networks between rhesus macaque and
359 human trophoblasts.
360

361 **Discussion**

362 Existing *in vitro* models fail to reflect the cellular complexity of the rhesus macaque
363 placenta. In this study, we established and characterized rhesus macaque placental organoids
364 using immunostaining, bulk RNA-sequencing, and single-cell RNA sequencing, providing a

365 detailed transcriptional profile of primate placentation. Our findings demonstrate that rTOs
366 recapitulate the transcriptional signatures and secretory phenotypes of the rhesus macaque
367 placenta. Single-cell RNA-seq revealed that these organoids can differentiate into distinct
368 trophoblast lineages, allowing us to identify and define specific markers for rhesus macaque
369 trophoblast populations. This model enables comparative analysis of rhesus macaque and human
370 trophoblasts. Through single-cell trajectory analysis, we uncovered distinct STB differentiation
371 trajectories between the two species. Lastly, we defined the intra- and inter-trophoblast
372 communication networks between the human and rhesus macaque placentas, which revealed
373 conserved and species-specific signaling pathways. Collectively, these findings provide valuable
374 insights into rhesus macaque trophoblast transcriptional profiles and new models for investigating
375 primate placentation.

376 Comparisons of many *in vitro* models of human trophoblasts to *in vivo* tissue have
377 revealed the limitations of these models[23]. For example, while monolayer cell lines (e.g. BeWo,
378 JEG-3, and JAR) are easy to culture, they are tumor-derived and do not spontaneously
379 differentiate into multiple trophoblast lineages. While primary human trophoblasts do differentiate
380 (e.g., to form fused STB), they have limited proliferation capability and a short life span in cell
381 culture. TSC models overcome many of these limitations but require exogenous agents (e.g.,
382 forskolin) for proliferative trophoblasts to differentiate into specific trophoblast populations,
383 particularly when grown in two-dimensions. Previously described human trophoblast and decidua
384 organoids have provided a physiologically relevant model of the maternal-fetal interface that is
385 able to spontaneously differentiate into distinct trophoblast lineages and recapitulate the
386 transcriptional profile of placental tissue across gestation[8,10,11]. Of note, hTOs derived from late
387 gestation placental tissue more closely recapitulate the transcriptional signature of the first
388 trimester placenta[10]. It remains uncertain whether the rTOs described here accurately replicate
389 the rhesus macaque placenta during the first trimester. Comparative studies to address this
390 question are challenging due to the limited accessibility of this tissue. However, mCG secretion in

391 macaques occurs only during the early stages of pregnancy and is undetectable after day 40,
392 suggesting that rTOs most likely resemble the first trimester placenta, as we observed mCG
393 secretion.

394 There is currently no consensus on confirmed EVT markers in the rhesus macaque
395 placenta. Previous studies have shown that many human-associated EVT markers are present in
396 STB cells in rhesus macaques, complicating the identification of true EVT markers in this species
397 [13]. This underscores the species-specific differences in gene expression between rhesus
398 macaque and human placentas. Thus, organoid models provide a critical tool for cross-species
399 comparisons of specific trophoblast cell types, enabling a deeper understanding of the unique
400 and shared aspects of trophoblast biology in different primates. These models will allow for more
401 accurate characterization of EVT and other trophoblast populations in rhesus macaques and
402 facilitate the identification of reliable markers, which could help to resolve the current uncertainty
403 in the field. Further studies, particularly those using single-cell trajectory analysis and optimized
404 approaches to drive EVT differentiation in rTOs, are needed to confirm the differentiation
405 pathways and molecular signatures of EVT populations in the rhesus macaque. This cross-
406 species approach is essential for advancing our understanding of placental development and
407 function in primates.

408 In both rhesus macaque and human placentas, the STB plays a critical role in nutrient
409 exchange, hormone production, and immune protection by forming the outermost cell layer of the
410 placenta that interfaces with maternal blood. While the overall function of the STB is conserved
411 across both species, there are differences in structure and cellular dynamics. In humans, the
412 STB is characterized by an extensive, highly vascularized surface area with numerous microvilli
413 and a uniform, thin multinucleated layer, optimizing nutrient and gas exchange. In contrast, the
414 rhesus macaque STB has a slightly less extensive surface area with a change in phenotype that
415 occurs after implantation has begun[24]. These differences reflect species-specific adaptations in
416 placental structure and function. Our findings demonstrate both similarities and differences in the

417 gene expression profiles of the STB between rhesus macaques and humans. We observed the
418 expression of canonical markers of the STB, including HOPX, PGF, and HMOX1, in both rhesus
419 macaque- and human-derived organoids. These markers, known for their roles in trophoblast
420 function and placental development, were consistently present across both species, underscoring
421 the conserved nature of STB gene expression across species. Despite conservation of select
422 canonical markers, we also identified divergence in the transcriptional profiles of the STB between
423 rhesus macaque and humans. For example, while PAGE4 is a known CTB marker in the human
424 placenta, its expression increased along the STB trajectory in rTOs[25]. Additionally, genes such as
425 WNT5A and NGF, which are involved in STB differentiation in rhesus macaques, were not
426 observed in humans. These genes have been shown to be upregulated in the rhesus macaque
427 placenta compared to the human placenta[3]. These findings highlight the complex interplay
428 between conserved functions and species-specific adaptations in the STB, which might provide
429 valuable insights into the evolutionary pressures shaping placental biology and offering new
430 models for further comparative studies.

431 Placental genes and signaling pathways are conserved along primates, but differences in
432 gene expression have been observed associated with placental development[3]. While the
433 placentas of rhesus macaques and humans are both hemochorial and discoid, there are
434 differences in their development and structure. A key difference is the trophoblast invasion in the
435 rhesus macaque placenta compared to the human placenta. EVT invasion is crucial for anchoring
436 the placenta to the uterine wall and remodeling maternal blood vessels to ensure adequate blood
437 supply to the fetus in both rhesus macaque and human placentas. However, in humans, EVT
438 invasion is more extensive, penetrating deep into the decidua and myometrium, whereas in
439 rhesus macaques, the invasion is restricted and localized, reflecting species-specific adaptations
440 in placental structure and function[24,26]. These structural differences in EVTs may stem from distinct
441 gene expression profiles and signaling cues between rhesus macaque and human trophoblasts.
442 For instance, in humans, CCL5 is secreted at the maternal-fetal interface, and its receptor is

443 expressed on EVTs, playing a crucial role in regulating EVT invasion[27,28]. Our findings align with
444 this, as hTOs displayed high CCL5 expression specifically in the STB population, while it was
445 absent in rTOs. This difference in CCL5 signaling may contribute to the observed variations in
446 EVT structure and function between the two species. Overall, these findings underscore the
447 evolutionary adaptations in placental development and function that have driven species-specific
448 reproductive strategies and suggest that species-specific organoids can serve as powerful tools
449 to elucidate these unique mechanisms.

450 The studies presented here establish *in vitro* models that enable the detailed
451 characterization of transcriptional profiles in rhesus macaque placental cell types. Our findings
452 reveal cell-type specific differences between rhesus macaque and human trophoblasts, offering
453 new insights into species-specific placental biology. The ability to compare human and rhesus
454 macaque trophoblast organoids provides a powerful platform to explore the evolutionary
455 adaptations that have shaped placental development across species. Leveraging these organoids
456 will allow for a better understanding of the divergent and conserved mechanisms underlying
457 placental function, offering a unique perspective on the evolution of reproductive strategies in
458 primates.

459

460 **Acknowledgements**

461 This work was supported by the NIH grant AI145828 (C.B.C.), P01AI129859 (A.K. and C.B.C.),
462 and the Tulane National Primate Research Center (TNPRC) NIH Base Grant P51OD011104;
463 RRID: SCR_008167. We also gratefully acknowledge the Duke Light Microscopy Core Facility,
464 Duke Center for Genomic and Computational Biology (GCB), Duke Proteomics and Metabolomics
465 Core, the University of Wisconsin National Primate Research Center, and the Veterinary Medicine
466 staff at TNPRC.

467

468 **Materials and Methods**

469

470 **Rhesus macaque samples.** Placental tissues were obtained at Caesarian section from seven
471 third trimester pregnant Indian-ancestory rhesus macaques housed at the Tulane National
472 Primate Research Center (TNPRC). The pregnant females included five rhesus cytomegalovirus
473 (RhCMV)- seronegative dams experimentally infected with two RhCMV strains in early second
474 trimester gestation, and two RhCMV-seropositive dams that were experimentally depleted of
475 either CD8+ T-lymphocytes or CD20+ B-lymphocytes in late first trimester gestation. All animals
476 remained healthy until the time of elective Caesarian section conducted between 141-154
477 gestation days. All macaques were from the specific pathogen free breeding colony at TNPRC
478 and free of SIV, STLV, Type D retrovirus and herpes B virus. The study was approved by the
479 TNPRC Institutional Animal Care and Use Committee (IACUC) and conducted in accordance with
480 the Guide for the Care and Use of Laboratory Animals at the NIH.

481

482 **Human samples.** Human tissue used in this study was obtained from Duke University after
483 approval was received from the Duke University Institutional Review Board (IRB) and in
484 accordance with the guidelines of Duke University human tissue procurement. Human placental
485 tissue used in this study for the generation of organoids was collected from third trimester ($38^{th}$-
486 $41^{st}$ weeks) from Caesarean sections. Tissue was collected from healthy normal donors and
487 tissue was excluded in cases of fetal anomalies or aneuploidy.

488

489 **Derivation and culture of organoids from human and rhesus macaque placental samples.**
490 Placental tissue was carefully dissected and separated into chorionic villi, smooth chorion,
491 amnion, and decidua separated. The amnion layer was kept intact and peeled from the chorion.
492 To remove decidua from the chorion, isolated chorion tissue was carefully scraped with forceps.
493 Stem/progenitor cells isolation from smooth chorion were similar to full-term chorionic villous
494 isolation previously described[10]. Briefly, dissected tissue was cut into small pieces (1-2$mm^2$) and

495 sequentially digested with 0.2% trypsin-250 (Alfa Aesar, J63993-09)/0.02% EDTA (Sigma-Aldrich
496 E9884-100G) and 1.0 mg/mL collagenase V (Sigma-Aldrich, C9263-100MG) on a 37°C stir plate
497 in small bottles containing stir bars. After the collagenase V digestion, tissue was disrupted
498 manually by vigorous pipetting with a 5-10mL serological pipette (10-20 times) prior to filtration.
499 Then pool two digests flow-through and pellet by centrifugation (600g for 6 minutes) and finally
500 resuspend with ice-cold growth-factor-reduced Matrigel (Corning 356231). Matrigel "domes"
501 (40ul/well) were plated into 24-well tissue culture plates (Corning 3526), placed in a 37°C
502 incubator to pre-polymerize for approximately 3 minutes, turned upside down to ensure equal
503 distribution of the isolated cells in domes for another 10 minutes, then carefully overlaid with 500
504 μL prewarmed media. For both rTOs and hTOs derivation and culture, the term trophoblast
505 organoid medium (tTOM) consisting of Advanced DMEM/F12 (Life Technologies, 12634-010)
506 supplemented with 1× B27 (Life Technologies, 17504-044), 1× N2 (Life Technologies, 17502-
507 048), 10% FBS (vol/vol, Cytiva HyClone, SH30070.03), 2 mM GlutaMAX™ supplement (Life
508 Technologies, 35050-061), 100 μg/mL Primocin (InvivoGen, ant-pm-1), 1.25 mM N-Acetyl-L-
509 cysteine (Sigma, A9165), 500 nM A83-01 (Tocris, 2939), 1.5 μM CHIR99021 (Tocris, 4423), 50
510 ng/mL recombinant human EGF (Gibco, PHG0314), 80 ng/mL recombinant human R-spondin 1
511 (R & D systems, 4645-RS-100), 100 ng/mL recombinant human FGF2 (Peprotech, 100-18C), 50
512 ng/mL recombinant human HGF (Peprotech, 100-39), 10mM nicotinamide (Sigma, N0636-100G),
513 5 μM Y-27632 (Sigma, Y0503-1MG), and 2.5 μM prostaglandin E2 (PGE2, R & D systems, 22-
514 961-0) was used. To passage, TOs were digested in prewarmed TrypLE Express (Gibco, 12605-
515 028) at 37°C for 8 min. Further mechanical dissociation was achieved by manual disruption.
516 Dissociated TOs were collected and washed by centrifuge, then resuspended in fresh ice-cold
517 Matrigel and replated as domes at the desired density for continuous culture. For freezing,
518 overlaid media was aspirated, and organoid-Matrigel domes were resuspended in CryoStor CS10
519 stem cell freezing medium (STEMCell Technologies, 07930) and frozen at -80 ℃ and then

520 transferred to liquid nitrogen for long-term storage. For thawing cryopreserved TOs, organoids
521 were thawed as quickly as possible, diluted with 5 times volume of basic TOM containing
522 Advanced DMEM/F12, 2 mM GlutaMAX supplement, 10 mM HEPES (Gibco, 15630-106), 1 ×
523 Penicillin/Streptomycin (Lonza, 17-602E) and centrifuged to pellet. Afterwards, TOs were
524 resuspended in new ice-cold Matrigel and replated for recovery culture and passaged as
525 described above.
526
527 **Derivation and culture of organoids from human and rhesus macaque decidua samples.**
528 Decidual tissue was dissected from human and rhesus macaque placenta, and further cleaned
529 by removing as much as possible those attached chorionic villi prior to the isolation of decidua
530 glands-enriched suspension as described previously (Turco et al., 2017b; Turco et al., 2017a,
531 Yang et al., 2022). Briefly, collected decidual tissues were cut into small pieces then digested in
532 1.25 U/mL Dispase II (Sigma-Aldrich, D4693)/0.4mg/mL collagenase V (Sigma-Aldrich, C-9263).
533 Following digestion and pipetting, the decidua glandular structures were filtered out with 100 μm
534 cell strainer, then collect the glandular structures from strainer and pipette to dissociate them into
535 small pieces before resuspending with ice-cold growth-factor-reduced Matrigel (Corning 356231),
536 plated as “domes” in 24-well plates (Corning, 3526), and overlaid with 500 μL prewarmed media.
537 For decidua organoids Expansion Medium (ExM) was used with the same composition as
538 previously described[29]. ExM was renewed every 2-3 days. Mature decidua organoids were
539 passaged by mechanical disruption following TrypLE Express (ThermoFisher Scientific,
540 12605010) digestion.
541
542 **Generation of conditioned media.** Overlaid media was collected from mature organoids after 7-
543 10 days post-passaging. CM was stored at -20°C. Non-conditioned medium (NCM) was TOM

544 (described above) that had not been exposed to organoids. All experiments using CM were from
545 at least two independent TO lines.
546
547 **Hormone Secretion Assays.** Conditioned media was collected as described above and a
548 radioimmunoassay was used to quantify mCG and progesterone secretion in cell conditioned
549 media as previously described[16,17].
550
551 **Mass Spectrometry.** CM was collected from rTOs and submitted to Duke University Proteomics
552 and Metabolomics Core Facility. SDS-PAGE gel bands were subjected to in-gel tryptic digestion
553 using standardized protocols[30]. Digested peptides were lyophilized to dryness and resuspended
554 in 12 uL of 0.2% formic acid/2% acetonitrile. Each sample was subjected to chromatographic
555 separation on a Thermo Neo Vanquish UPLC equipped with a 1.7 $\mu$m HSS T3 C18 75 $\mu$m I.D. X
556 250 mm reversed-phase column (NanoFlow data). The mobile phase consisted of (A) 0.1% formic
557 acid in water and (B) 0.1% formic acid in acetonitrile. 3 $\mu$L was injected and peptides were trapped
558 for 3 min on a 5 $\mu$m Symmetry C18 180 $\mu$m I.D. X 20 mm column at 5 $\mu$l/min in 99.9% A. The
559 analytical column was then switched in-line and a linear elution gradient of 5% B to 40% B was
560 performed over 30 min at 400 nL/min. Data collection on the Fusion Lumos mass spectrometer
561 with a FAIMS Pro device was performed for three difference compensation voltages (-40v, -60v,
562 -80v). Within each CV, a data-dependent acquisition (DDA) mode of acquisition with a r=120,000
563 (@ m/z 200) full MS scan from m/z 375 - 1500 with a target AGC value of 4e5 ions was performed.
564 MS/MS scans with HCD settings of 30% were acquired in the linear ion trap in "rapid" mode with
565 a target AGC value of 1e4 and max fill time of 35 ms. The total cycle time for each CV was 0.66s,
566 with total cycle times of 2 sec between like full MS scans. A 20s dynamic exclusion was employed
567 to increase depth of coverage.

568 Raw LC-MS/MS data files were processed in Proteome Discoverer 3.0 (Thermo Scientific)
569 and then submitted to independent Sequest database searches against a Rhesus Macaque
570 protein database containing both forward (20260 entries) and reverse entries of each
571 protein. Search tolerances were 2 ppm for precursor ions and 0.8 Da for product ions using
572 trypsin specificity with up to two missed cleavages. All searched spectra were imported into
573 Scaffold (v5.3, Proteome Software) and scoring thresholds were set to achieve a peptide false
574 discovery rate of 1% using the PeptideProphet algorithm. Raw data were also imported into
575 Protein Discoverer 3.0 for area under the curve measurements of eluting peptides.
576
577 **Immunofluorescence.** Organoids were fixed in 4% PFA for 15 min at room temperature, then
578 washed in PBS. Organoids were placed in 0.25% Triton X-100/PBS to permeabilize for 15 min at
579 room temperature. Organoids were washed in 1x PBS and then incubated with the indicated
580 primary antibodies in PBS at 4°C overnight. Organoids were pelleted by gravity, washed with PBS,
581 and then incubated for 30 min at room temperature with Alexa Fluor-conjugated secondary
582 antibodies (Invitrogen). Organoids were washed again with PBS and mounted in Vectashield
583 (Vector Laboratories) containing 4′,6-diamidino- 2-phenylindole (DAPI) and were transferred onto
584 microscope slides with large-orifice 200 µL-tips (Fisher Scientific, 02707134). The following
585 antibodies and reagents were used: cytokeratin-19 (Abcam, ab9221, ab52625), SDC-1 (abcam,
586 ab128936), ITGA6 (Invitrogen, MA5-16884), E-cadherin (Invitrogen, PA5-85088), Mucin 5AC
587 (Abcam, ab3649), Alexa Fluor 594–conjugated phalloidin (Invitrogen, A12381).
588
589 **RNA extraction and Bulk RNA-seq.** Total RNA was isolated with the Sigma GenElute total
590 mammalian RNA miniprep kit or Qiagen RNAeasy Mini Kit following the manufacturer's instruction
591 and using supplementary Sigma DNase digestion. RNA quality and concentration were
592 determined using a Nanodrop ND-1000 Spectrophotometer. For bulk RNA-seq analysis, RNA was

593 isolated from organoids or placenta tissue as described above. Purified Total RNA was verified by
594 Thermo scientific Nanodrop one. The libraries were prepared by the Duke Center for Genomic
595 and Computational Biology (GCB) using the Tru-Seq stranded total RNA prep kit (Illumina).
596 Sequencing was performed on the NovaSeq 6000 by using 150-bp paired-end sequencing. The
597 reads were aligned to the human or rhesus macaque reference genome (GRCh38, Mmul10) using
598 QIAGEN CLC Genomics (v20). Differential expression analysis was performed using the DeSeq2
599 package in R [31], k-means pathway cluster enrichment for GO Biological processes and principal
600 component analyses (PCA) was performed using iDEP [32,33]. Heatmaps and hierarchical clustering
601 was performed in R using the pheatmap package and were based on $\log_2$ RPKM (reads per
602 kilobase million). Files associated with bulk RNA-seq studies have been deposited into Sequence
603 Read Archive (PRJNA891648). Principal component analyses were performed using pcaExplorer
604 in R [34]. Volcano plots were generated using the EnhancedVolcano package in R or in Graphpad
605 Prism version 9.
606
607 **Dissociation of organoids for single cell RNA sequencing.** Organoids were dissociated by
608 scraping Matrigel domes into 1 mL of pre-warmed TrypLE Express (Invitrogen, 12605036) and
609 incubating at 37ºC for 12 min, swirling the tube every 2-3 min. Dissociated organoids were
610 pelleted at 1250 rpm for 3 min and re-suspended in 200 µL DMEM containing 10% FBS.
611 Resuspended organoids were subjected to vigorous manual disruption using a single channel
612 p200 pipette (Ranin, 17008652) for 3 min followed by the addition of 800 µL of DMEM containing
613 10% FBS. The disrupted suspension was then passed over a 40 µm filter cell strainer (Corning,
614 352098). Flow through was then centrifuged at 1250 rpm for 5min and the pellet resuspended in
615 250 µL of 1x PBS for a final volume of ~300 µL and cell counts of ~1 x $10^6$ cells/mL. Cell viability
616 was determined using trypan blue and followed by automated cell counting (Biorad TC20
617 automated cell counter), with all samples containing ~80% minimum viability. Sequencing was
618 performed on two organoid lines from unique placental tissue.

619

620 **Single-Cell RNA-seq Library Preparation and Data Analysis.** Libraries were prepared from
621 10k total cells using the methods described in the 10x Genomics Single Cell 3' Reagent Kit
622 Protocol (v2 chemistry, Manual Part #CG00052). Sequencing runs were performed on an Illumina
623 NovaSeq 6000 (Illumina, San Diego) using an S2 flow cell (Illumina, San Diego), which allowed
624 for ~61k reads/cell. Post-processing, quality control, and read alignment to the Mmul10 rhesus
625 macaque reference genome or to the hg38 human reference genome were performed using 10x
626 CellRanger package (v6.1.2, 10x Genomics). Gene expression matrices generated by the 10x
627 CellRanger aggregate option were analyzed using Seurat (version 4.0) in R [35-38]. Cells with at
628 least 200 and no more than 10,000 unique expressed genes were included in downstream
629 analysis, and cells with more than 10% mitochondrial reads were excluded from analysis. To
630 eliminate batch effects, datasets from unique donors were normalized using the *sctransform*
631 function and integrated using the *FindIntegrationAnchors()* in Seurat (version 4.0) in R [38].
632 Dimensional reduction was performed using the *RunPCA()* function to obtain the first 20 principal
633 components, which was determined using *ElbowPlots()* across the first 50 dimensions. To identify
634 clusters, Louvain clustering (Seurat *FindClusters()* function) was performed, and optimal
635 resolution was determined using the *clustree()* function[39] on a range of resolutions between 0.2-
636 1.0, with 0.3 used for downstream analyses. Integration of rTO and hTO datasets was performed
637 on previously integrated datasets using the Harmony algorithm[40] (v1.0) for batch correction and
638 alignment. Differential expression analysis between clusters was performed using the Wilcoxon
639 rank sum test implemented in Seurat's FindAllMarkers() function. Genes with a log2 fold change
640 > 0.25 and an FDR-adjusted p-value < 0.05 were considered significantly differentially expressed.
641 Marker genes for each cluster were identified by searching for positively enriched genes using
642 the aforementioned criteria. All files associated with this single-cell RNA-seq study have been
643 deposited in the Gene Expression Omnibus (GEO).

The *slingshot* package (version 2.6.0) in R was used to determine differentiation trajectories from clusters identified in Seurat with unbiased starting and ending roots[20]. The raw counts and above-generated slingshot object were used to run *evaluateK()* with the total number of knots ranging from 3 to 9. The optimal number of knots was determined to be 4. The *fitGAM()* function using *tradeSeq* (1.5.10) was run with this resulting value and gene expression along lineages identified using the *associationTest()* function[41]. Heatmaps of expression changes across lineages were generated using *ComplexHeatmap()* on log transformed counts and rasterized using the *ImageMagick* "Bessel" filter [42]. The *plotGenePseudotime()* function was used to visualize raw count gene expression in individual cells across lineages from the *slingshot* object.

**Statistics and reproducibility.** All experiments reported in this study have been reproduced using independent samples (tissues and organoids) from multiple donors. All statistical analyses were performed using Prism software (GraphPad Software). Data are presented as mean ± SD, unless otherwise stated. Statistical significance was determined as described in the figure legends. Parametric tests were applied when data were distributed normally based on D'Agostino-Pearson analyses; otherwise, nonparametric tests were applied. For all statistical tests, p value $<0.05$ was considered statistically significant, with specific p values noted in the figure legends.

## Literature Cited


1. Carter, A.M., and Enders, A.C. (2004). Comparative aspects of trophoblast development and placentation. Reprod Biol Endocrinol *2*, 46. 10.1186/1477-7827-2-46.
2. de Rijk, E.P.C.T., and Van Esch, E. (2008). The Macaque Placenta-A Mini-Review. Toxicol Pathol *36*, 108s-118s. 10.1177/0192623308326095.
3. Rosenkrantz, J.L., Gaffney, J.E., Roberts, V.H.J., Carbone, L., and Chavez, S.L. (2021). Transcriptomic analysis of primate placentas and novel rhesus trophoblast cell lines informs investigations of human placentation. BMC Biol *19*, 127. 10.1186/s12915-021-01056-7.
4. Boyson, J.E., Iwanaga, K.K., Golos, T.G., and Watkins, D.I. (1996). Identification of the rhesus monkey HLA-G ortholog. Mamu-G is a pseudogene. J Immunol *157*, 5428-5437.
5. Brinkman-Van der Linden, E.C., Hurtado-Ziola, N., Hayakawa, T., Wiggleton, L., Benirschke, K., Varki, A., and Varki, N. (2007). Human-specific expression of Siglec-6 in the placenta. Glycobiology *17*, 922-931. 10.1093/glycob/cwm065.
6. Esnault, C., Cornelis, G., Heidmann, O., and Heidmann, T. (2013). Differential evolutionary fate of an ancestral primate endogenous retrovirus envelope gene, the EnvV syncytin, captured for a function in placentation. PLoS Genet *9*, e1003400. 10.1371/journal.pgen.1003400.
7. Maston, G.A., and Ruvolo, M. (2002). Chorionic gonadotropin has a recent origin within primates and an evolutionary history of selection. Mol Biol Evol *19*, 320-335. 10.1093/oxfordjournals.molbev.a004085.
8. Turco, M.Y., Gardner, L., Kay, R.G., Hamilton, R.S., Prater, M., Hollinshead, M.S., McWhinnie, A., Esposito, L., Fernando, R., Skelton, H., et al. (2018). Trophoblast organoids as a model for maternal-fetal interactions during human placentation. Nature *564*, 263-267. 10.1038/s41586-018-0753-3.
9. Haider, S., Meinhardt, G., Saleh, L., Kunihs, V., Gamperl, M., Kaindl, U., Ellinger, A., Burkard, T.R., Fiala, C., Pollheimer, J., et al. (2018). Self-Renewing Trophoblast Organoids Recapitulate the Developmental Program of the Early Human Placenta. Stem Cell Reports *11*, 537-551. 10.1016/j.stemcr.2018.07.004.
10. Yang, L., Semmes, E.C., Ovies, C., Megli, C., Permar, S., Gilner, J.B., and Coyne, C.B. (2022). Innate immune signaling in trophoblast and decidua organoids defines differential antiviral defenses at the maternal-fetal interface. Elife *11*. 10.7554/eLife.79794.
11. Keenen, M.M., Yang, L., Liang, H., Farmer, V.J., Singh, R., Gladfelter, A.S., and Coyne, C.B. (2024). Comparative analysis of the syncytiotrophoblast in placenta tissue and trophoblast organoids using snRNA sequencing. bioRxiv, 2024.2007.2001.601571. 10.1101/2024.07.01.601571.
12. Okae, H., Toh, H., Sato, T., Hiura, H., Takahashi, S., Shirane, K., Kabayama, Y., Suyama, M., Sasaki, H., and Arima, T. (2018). Derivation of Human Trophoblast Stem Cells. Cell Stem Cell *22*, 50-63 e56. 10.1016/j.stem.2017.11.004.
13. Schmidt, J.K., Keding, L.T., Block, L.N., Wiepz, G.J., Koenig, M.R., Meyer, M.G., Dusek, B.M., Kroner, K.M., Bertogliat, M.J., Kallio, A.R., et al. (2020). Placenta-derived macaque trophoblast stem cells: differentiation to syncytiotrophoblasts and extravillous trophoblasts reveals phenotypic reprogramming. Sci Rep *10*, 19159. 10.1038/s41598-020-76313-w.
14. Wang, M., Liu, Y., Sun, R., Liu, F., Li, J., Yan, L., Zhang, J., Xie, X., Li, D., Wang, Y., et al. (2024). Single-nucleus multi-omic profiling of human placental syncytiotrophoblasts identifies cellular trajectories during pregnancy. Nat Genet *56*, 294-305. 10.1038/s41588-023-01647-w.
15. Shimizu, K. (2008). Reproductive Hormones and the Ovarian Cycle in Macaques. Journal of Mammalian Ova Research *25*, 122-126.

16. Block, L.N., Aliota, M.T., Friedrich, T.C., Schotzko, M.L., Mean, K.D., Wiepz, G.J., Golos, T.G., and Schmidt, J.K. (2020). Embryotoxic impact of Zika virus in a rhesus macaque in vitro implantation modeldagger. Biol Reprod *102*, 806-816. 10.1093/biolre/ioz236.
17. Ziegler, T.E., Matteri, R.L., and Wegner, F.H. (1993). Detection of urinary gonadotropins in callitrichid monkeys with a sensitive immunoassay based upan a unique monoclonal antibody. Am J Primatol *31*, 181-188. 10.1002/ajp.1350310303.
18. Moore, T., Williams, J.M., Becerra-Rodriguez, M.A., Dunne, M., Kammerer, R., and Dveksler, G. (2022). Pregnancy-specific glycoproteins: evolution, expression, functions and disease associations. Reproduction *163*, R11-R23. 10.1530/REP-21-0390.
19. Matsumoto, S., Porter, C.J., Ogasawara, N., Iwatani, C., Tsuchiya, H., Seita, Y., Chang, Y.W., Okamoto, I., Saitou, M., Ema, M., et al. (2020). Establishment of macaque trophoblast stem cell lines derived from cynomolgus monkey blastocysts. Sci Rep *10*, 6827. 10.1038/s41598-020-63602-7.
20. Street, K., Risso, D., Fletcher, R.B., Das, D., Ngai, J., Yosef, N., Purdom, E., and Dudoit, S. (2018). Slingshot: cell lineage and pseudotime inference for single-cell transcriptomics. BMC Genomics *19*, 477. 10.1186/s12864-018-4772-0.
21. Yu, G., Wang, L.G., Han, Y., and He, Q.Y. (2012). clusterProfiler: an R package for comparing biological themes among gene clusters. OMICS *16*, 284-287. 10.1089/omi.2011.0118.
22. Jin, S., Guerrero-Juarez, C.F., Zhang, L., Chang, I., Ramos, R., Kuan, C.H., Myung, P., Plikus, M.V., and Nie, Q. (2021). Inference and analysis of cell-cell communication using CellChat. Nat Commun *12*, 1088. 10.1038/s41467-021-21246-9.
23. Li, X., Li, Z.H., Wang, Y.X., and Liu, T.H. (2023). A comprehensive review of human trophoblast fusion models: recent developments and challenges. Cell Death Discov *9*, 372. 10.1038/s41420-023-01670-0.
24. Carter, A.M., Enders, A.C., and Pijnenborg, R. (2015). The role of invasive trophoblast in implantation and placentation of primates. Philos Trans R Soc Lond B Biol Sci *370*, 20140070. 10.1098/rstb.2014.0070.
25. Marsh, B., Zhou, Y., Kapidzic, M., Fisher, S., and Blelloch, R. (2022). Regionally distinct trophoblast regulate barrier function and invasion in the human placenta. Elife *11*. 10.7554/eLife.78829.
26. Enders, A.C., Lantz, K.C., and Schlafke, S. (1996). Preference of invasive cytotrophoblast for maternal vessels in early implantation in the macaque. Acta Anat (Basel) *155*, 145-162. 10.1159/000147800.
27. Li, Q., Sharkey, A., Sheridan, M., Magistrati, E., Arutyunyan, A., Huhn, O., Sancho-Serra, C., Anderson, H., McGovern, N., Esposito, L., et al. (2024). Human uterine natural killer cells regulate differentiation of extravillous trophoblast early in pregnancy. Cell Stem Cell *31*, 181-195 e189. 10.1016/j.stem.2023.12.013.
28. Wei, X.W., Zhang, Y.C., Wu, F., Tian, F.J., and Lin, Y. (2022). The role of extravillous trophoblasts and uterine NK cells in vascular remodeling during pregnancy. Front Immunol *13*, 951482. 10.3389/fimmu.2022.951482.
29. Turco, M.Y., Gardner, L., Hughes, J., Cindrova-Davies, T., Gomez, M.J., Farrell, L., Hollinshead, M., Marsh, S.G.E., Brosens, J.J., Critchley, H.O., et al. (2017). Long-term, hormone-responsive organoid cultures of human endometrium in a chemically defined medium. Nat Cell Biol *19*, 568-577. 10.1038/ncb3516.
30. Wilm, M., Shevchenko, A., Houthaeve, T., Breit, S., Schweigerer, L., Fotsis, T., and Mann, M. (1996). Femtomole sequencing of proteins from polyacrylamide gels by nano-electrospray mass spectrometry. Nature *379*, 466-469. 10.1038/379466a0.
31. Love, M.I., Huber, W., and Anders, S. (2014). Moderated estimation of fold change and dispersion for RNA-seq data with DESeq2. Genome Biol *15*, 550. 10.1186/s13059-014-0550-8.

32. Ge, S.X., Son, E.W., and Yao, R. (2018). iDEP: an integrated web application for differential expression and pathway analysis of RNA-Seq data. BMC Bioinformatics *19*, 534. 10.1186/s12859-018-2486-6.
33. Ge, X. (2021). iDEP Web Application for RNA-Seq Data Analysis. Methods Mol Biol *2284*, 417-443. 10.1007/978-1-0716-1307-8_22.
34. Marini, F., and Binder, H. (2019). pcaExplorer: an R/Bioconductor package for interacting with RNA-seq principal components. BMC Bioinformatics *20*, 331. 10.1186/s12859-019-2879-1.
35. Hao, Y., Hao, S., Andersen-Nissen, E., Mauck, W.M., 3rd, Zheng, S., Butler, A., Lee, M.J., Wilk, A.J., Darby, C., Zager, M., et al. (2021). Integrated analysis of multimodal single-cell data. Cell *184*, 3573-3587 e3529. 10.1016/j.cell.2021.04.048.
36. Butler, A., Hoffman, P., Smibert, P., Papalexi, E., and Satija, R. (2018). Integrating single-cell transcriptomic data across different conditions, technologies, and species. Nat Biotechnol *36*, 411-420. 10.1038/nbt.4096.
37. Satija, R., Farrell, J.A., Gennert, D., Schier, A.F., and Regev, A. (2015). Spatial reconstruction of single-cell gene expression data. Nat Biotechnol *33*, 495-502. 10.1038/nbt.3192.
38. Stuart, T., Butler, A., Hoffman, P., Hafemeister, C., Papalexi, E., Mauck, W.M., 3rd, Hao, Y., Stoeckius, M., Smibert, P., and Satija, R. (2019). Comprehensive Integration of Single-Cell Data. Cell *177*, 1888-1902 e1821. 10.1016/j.cell.2019.05.031.
39. Zappia, L., and Oshlack, A. (2018). Clustering trees: a visualization for evaluating clusterings at multiple resolutions. Gigascience *7*. 10.1093/gigascience/giy083.
40. Korsunsky, I., Millard, N., Fan, J., Slowikowski, K., Zhang, F., Wei, K., Baglaenko, Y., Brenner, M., Loh, P.R., and Raychaudhuri, S. (2019). Fast, sensitive and accurate integration of single-cell data with Harmony. Nat Methods *16*, 1289-1296. 10.1038/s41592-019-0619-0.
41. Van den Berge, K., Roux de Bezieux, H., Street, K., Saelens, W., Cannoodt, R., Saeys, Y., Dudoit, S., and Clement, L. (2020). Trajectory-based differential expression analysis for single-cell sequencing data. Nat Commun *11*, 1201. 10.1038/s41467-020-14766-3.
42. ImageMagick (2023). ImageMagick Studio LLC. . https://imagemagick.org.

**Figure 1**

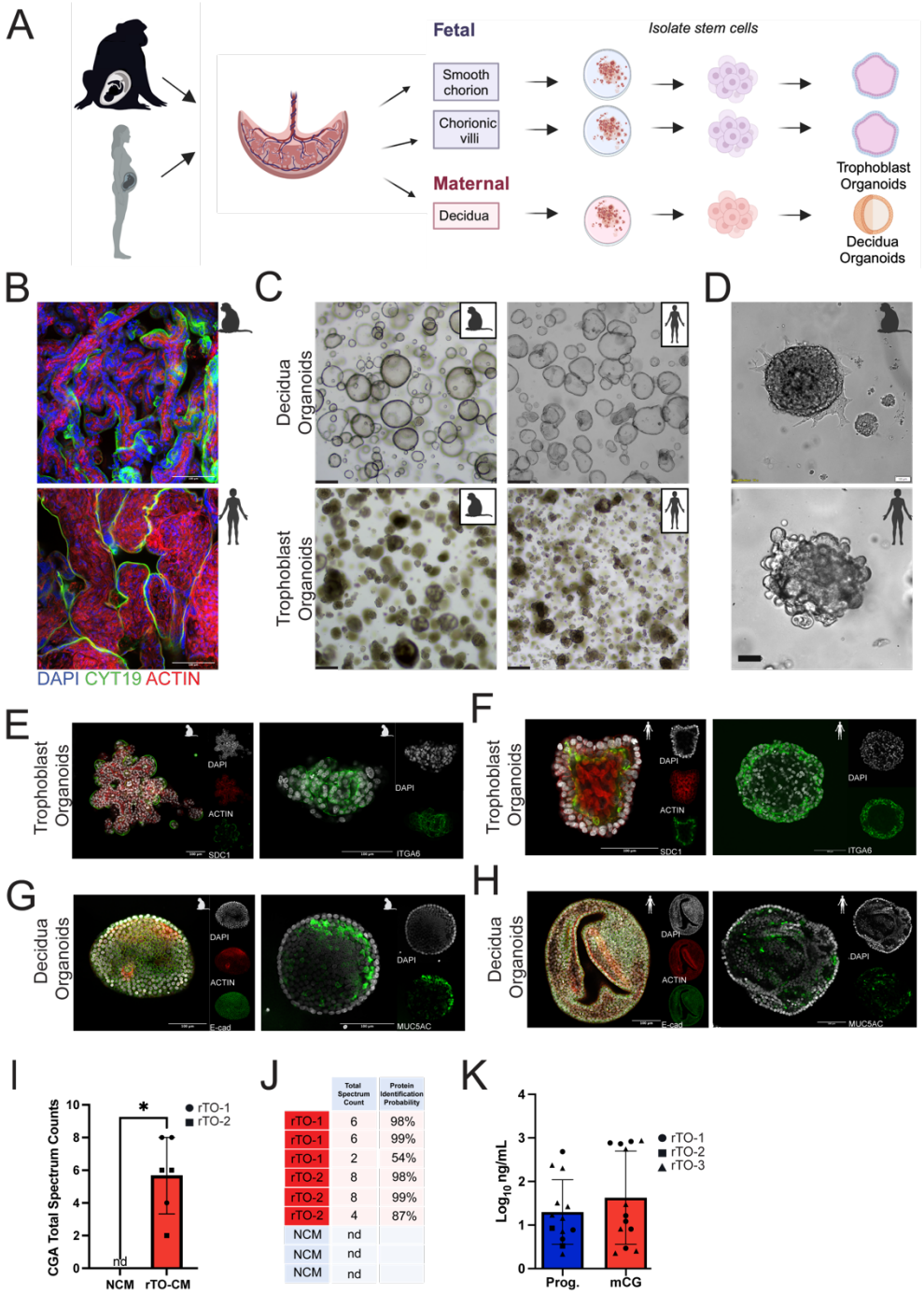


| | Total Spectrum Count | Protein Identification Probability |
|---|---|---|
| rTO-1 | 6 | 98% |
| rTO-1 | 6 | 99% |
| rTO-1 | 2 | 54% |
| rTO-2 | 8 | 98% |
| rTO-2 | 8 | 99% |
| rTO-2 | 4 | 87% |
| NCM | nd | |
| NCM | nd | |
| NCM | nd | |

**Figure 1. Establishment and of rhesus macaque trophoblast and decidua organoids. (A),** Schematic of the rhesus macaque and human placenta denoting full-term human and mid-late third trimester rhesus macaque fetal trophoblast and maternal decidua tissues used to generate matched organoids. Created using Biorender. **(B),** Confocal micrographs of rhesus macaque (top) and human (bottom) chorionic villi. Cytokeratin-19 is shown in green, actin is shown in red, and DAPI-stained nuclei are in blue. Scale bar, 100μm. **(C),** Top, brightfield images of representative

decidua organoids of rhesus macaque (left) and human (right). Bottom, representative brightfield images of trophoblast organoids of rhesus macaque (left) and human (right) trophoblast organoids. Scale bar, 500μm **(D),** Representative brightfield images of rTOs (top) and hTOs (bottom). Scale bar, 100μm. **(E, F),** Confocal micrographs of rTOs and hTOs immunostained for SDC1 (green), ACTIN (red), DAPI-stained nuclei are in black and white on the left, ITGA6 (green), DAPI-stained nuclei are in black and white on the right. Scale bar, 100μm. **(G, H),** Confocal micrographs of rDOs and hDOs immunostained for E-cadherin (green), ACTIN (red), DAPI-stained nuclei are in black and white on the left, MUC5AC (green), DAPI-stained nuclei are in black and white on the right. Scale bar, 100μm. **(I),** Total Spectrum Counts of Chorionic Gonadotropin (CGA) in non-conditioned media (NCM) and CM isolated from two independent lines of rTOs. Each point represents an independent replicate/well. **(J),** Quantification of total spectrum count and protein identification probability of mCG. **(K),** Secretion of progesterone and mCG from three unique rTO lines measured by radioimmunoassay. Each point represents an independent replicate/well.

871
872 **Figure 2**

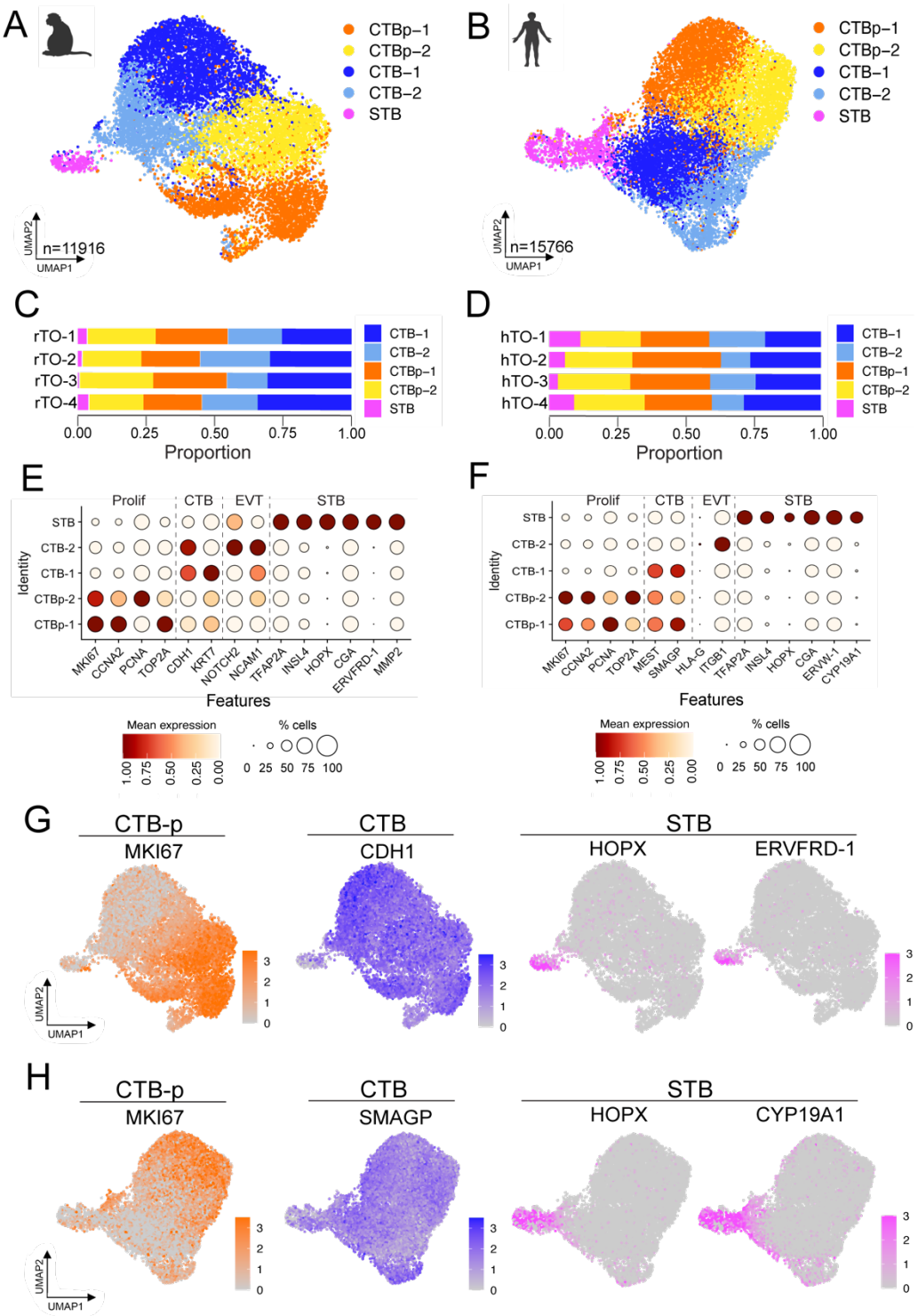


873
874
875 **Figure 2. Single cell RNA-seq defines trophoblast cell populations present in rhesus**
876 **macaque and human trophoblast organoids. (A, B),** UMAP of cell type clusters from four lines
877 of rhesus macaque (rTOs, A, n=11916 cells) and four lines of human (hTOs, D, n=15776 cells)
878 trophoblast organoids. Single-cell dataset generated from three unique lines of rTOs and four

unique lines of hTOs. Cell types are denoted as follows: cytotrophoblasts (CTB), proliferative cytotrophoblasts (CTB-p), extravillous trophoblasts (EVT), syncytiotrophoblasts (STB). Multiple clusters of one cell type are annotated using -number after the cell name. **(C, D),** Comparison of the enrichment of distinct cell clusters in rTOs (C) and hTOs (D). **(E, F),** Dot plots showing expression levels of indicated genes in each cluster in rTOs (E) and hTOs (F). The indicated genes are established markers for the syncytiotrophoblast (STB), cytotrophoblasts (CTBs), extravillous trophoblasts (EVTs) and trophoblast progenitor cells (CTB-p). Scale is shown at bottom. **(G, H),** Feature plots of trophoblast marker gene expression in rTOs (G) or hTOs (H). Scale is shown at right.

**Figure 3**

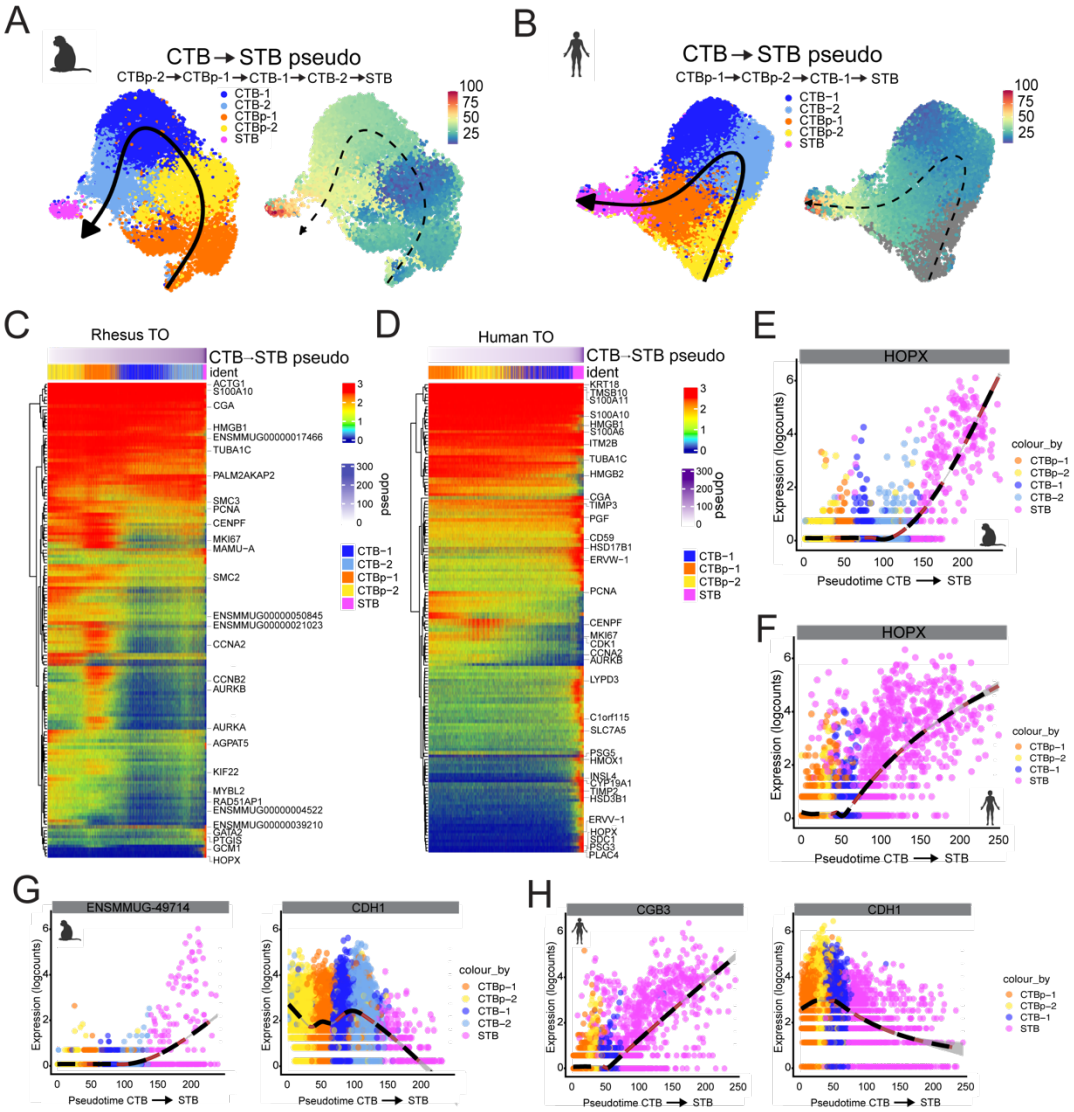


**Figure 3. Syncytiotrophoblast cell differentiation trajectory in rhesus and human trophoblast organoids.**

**(A,B),** Pseudotime was performed using Slingshot analysis to define cellular lineage reconstruction across datasets. This illustrates the trajectory of the cell types in the clusters in rTO (A, right) and hTO (B, right). Pseudotime values were assigned to each cell type and input into a color scale matching the UMAP based on time 0-100 in rTO (A, left) and hTO (B, left). The arrow across the UMAP shows the order of the trajectory. **(C, D),** Pseudotime values revealed top genes correlated to the trajectory in rTO (C) and hTO (D). **(E, F),** HOPX gene expression increases along the differentiation trajectory to STB subtype in rTO (E) and hTO (F). The cell types presented are represented by the colors denoted in the legend. Logcounts and pseudotime values are shown as a color scale present in the legend. **(G),** Normalized expression of ENSMMUG-49714and CDH1 shown along rTO pseudotime. **(H),** Normalized expression of CGB3 and CDH1 shown along hTO pseudotime.

**Figure 4**

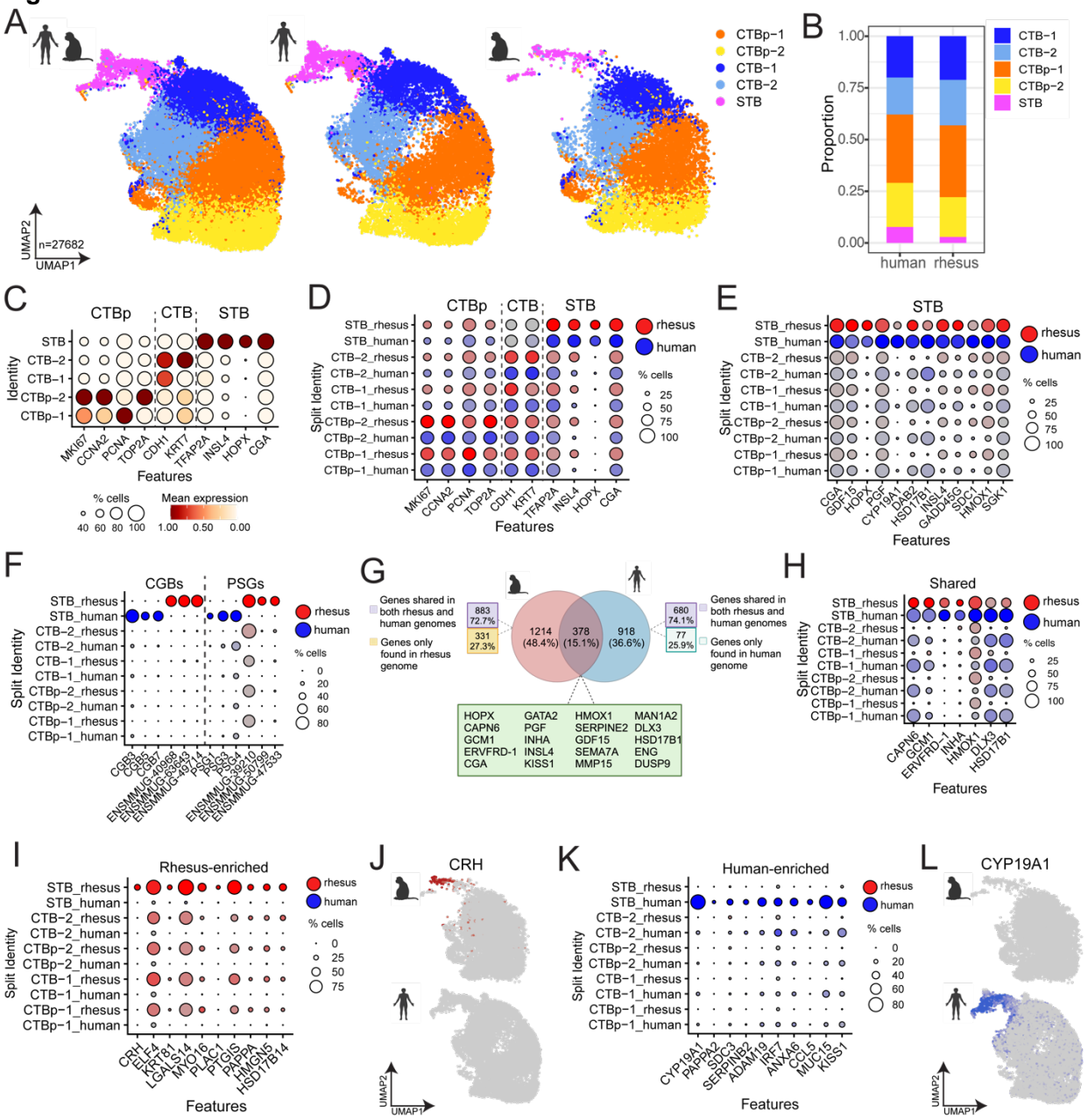


**Figure 4. Integrated analysis of rhesus macaque and human single cell RNA-seq identifies shared and distinct cellular transcriptional profiles. (A),** UMAP of merged cell type clusters from integrated datasets rTOs and hTOs (n=27,682 total cells). Three unique lines of rTOs and four unique lines of hTOs were used with four total samples from each species. Left, merged UMAP of clusters from rTOs and hTOs. Middle, cells from hTOs and right, cells from rTOs. **(B),** Cluster enrichment from hTO (left) and rTO (right) present in the integrated dataset. **(C),** Dot plots of canonical trophoblast markers in each cluster present in the integrated dataset. Key at bottom. **(D, E),** Canonical trophoblast markers in each cluster (D) or in the STB (E) present in the integrated dataset separated by species with rhesus in red and human in blue. Key at right. **(F),** Dot plots of rhesus macaque and human CGBs and PSGs (rhesus in red and human in blue). Key at right. **(G),** Venn diagram of markers in the rhesus and human STB clusters that identifies

shared and distinct markers. Markers that were shared are shown as genes that are present in both the rhesus macaque and human genome. Distinct rhesus and human STB markers include genes that are shared in the rhesus macaque and human genome as well as genes that are specific to one genome. **(H, I, J, K, L),** Dot plots of shared (H), rhesus-enriched (I) or human-enriched (K) markers found in the STB cluster separated by rTO and hTO conditions (rhesus in red and human in blue). Feature plot of CRH (J) and CYP19A1 (L) separated by rTO and hTO conditions.

**Figure 5**

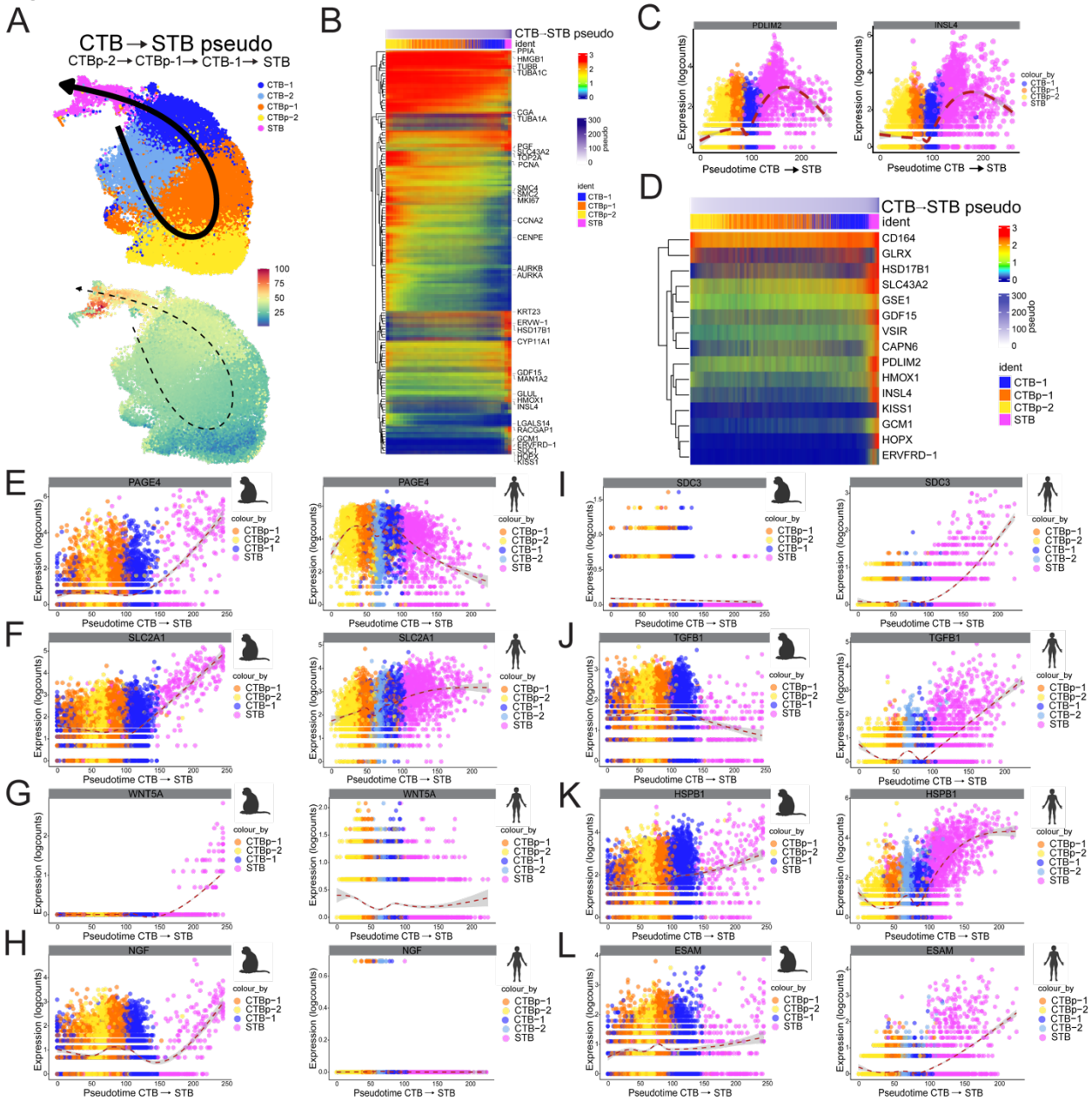


**Figure 5. Comparative single cell RNA-seq reveals distinct STB differentiation trajectories between human and rhesus macaque trophoblast organoids.**

**(A),** Pseudotime analysis of the integrated rTO and hTO datasets. The trajectory was mapped onto the UMAP, with pseudotime values assigned to each cell. These values were then visualized using a color scale corresponding to pseudotime progression from 0 to 100 across the integrated dataset. **(B),** Heatmap of the top genes associated with the pseudotime enriched in the combined rTO and hTO trajectory dataset. **(C),** Normalized expression of PDLIM2 and INSL4 shown along integrated pseudotime in the combined dataset. **(D),** Heatmap of genes that increase along the trajectory to the STB subtype in the integrated dataset. The cell types presented are represented by the colors denoted in the legend. Logcounts and pseudotime values are shown as a color scale present in the legend. **(E, F, G, H),** Normalized expression of PAGE4, SLC2A1, WNT5A, and NGF

shown across rTO (on left) and hTO (on right) trajectories. **(I, J, K, L),** Normalized expression of SDC3, TGFB1, HSPB1, and ESAM shown along rTO (on left) and hTO (on right) trajectories.

**Figure 6**

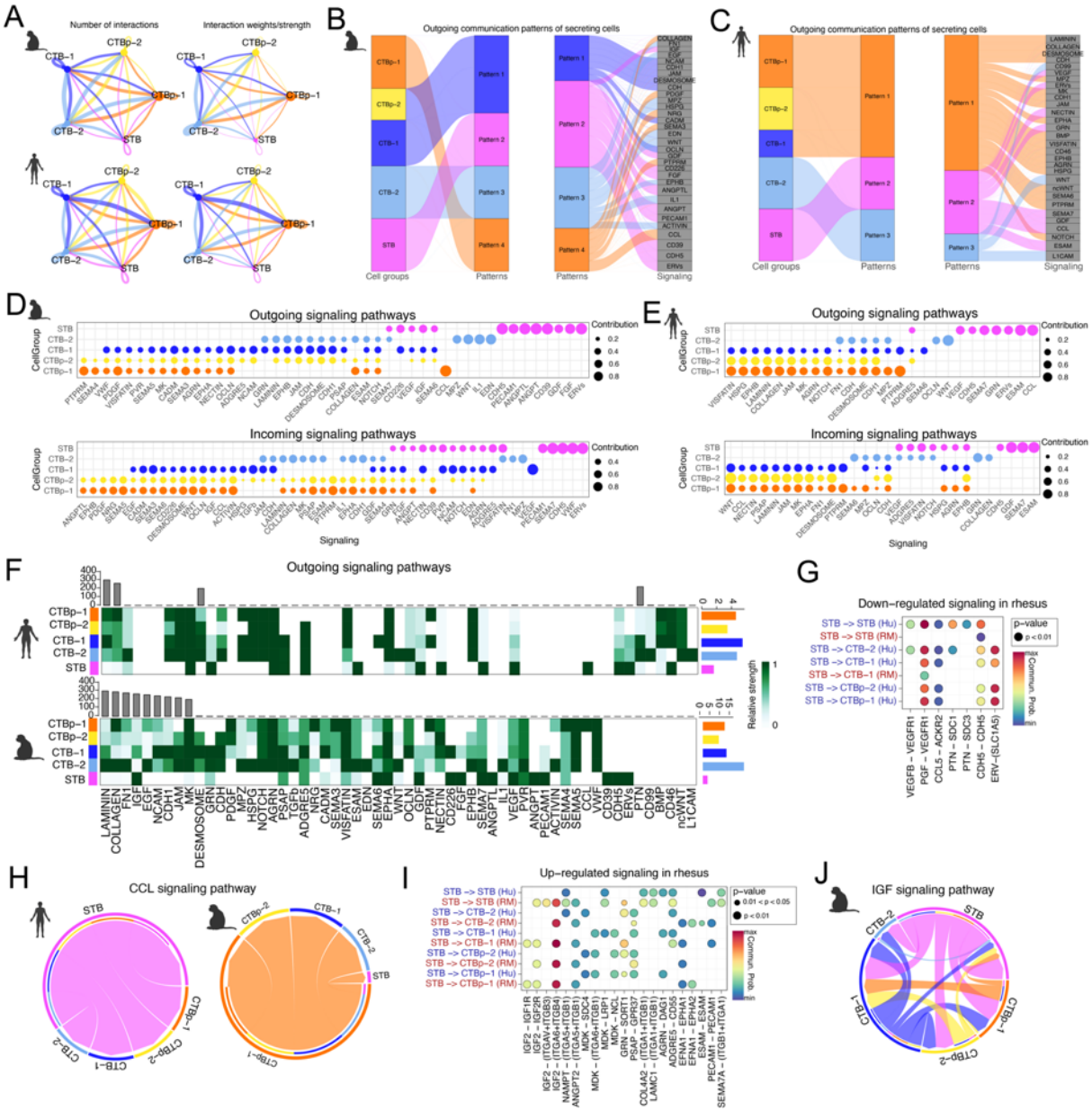


**Figure 6. Analysis of cell-cell communication networks in rTO and hTO. (A),** Ribbon plot of all cell-cell communication networks in rTO (top) and hTO (bottom). Plots on the left show the total number of interactions and plots on the right show the interaction strength among the cell clusters. **(B, C),** River plots of outgoing communications illustrating signals sent by sender cells correlating with signaling pathways in (B) rTOs and (C) hTOs. **(D, E),** Dot plot of total incoming (bottom) and outgoing (top) communication pathways of secreting cells based on clusters in rTO (left) and hTO (right). Key at right. **(F),** Heatmap of outgoing signals based on cell cluster in hTO (top) and rTO (bottom). The relative signaling strength is shown by the colorbar. Overall signaling strength of signaling pathway from each cluster is shown by bar plot at right. Key at right. **(G),** Dot plots of pathways down-regulated in rTOs relative to hTOs. Key at right. **(H),** Chord diagram of CCL signaling pathway in rTO and hTO. **(I),** Dot plots of pathways up-regulated in rTOs relative to hTOs. Key at right **(J),** Chord diagram of IGF signaling pathway in rTOs.

**Figure S1**

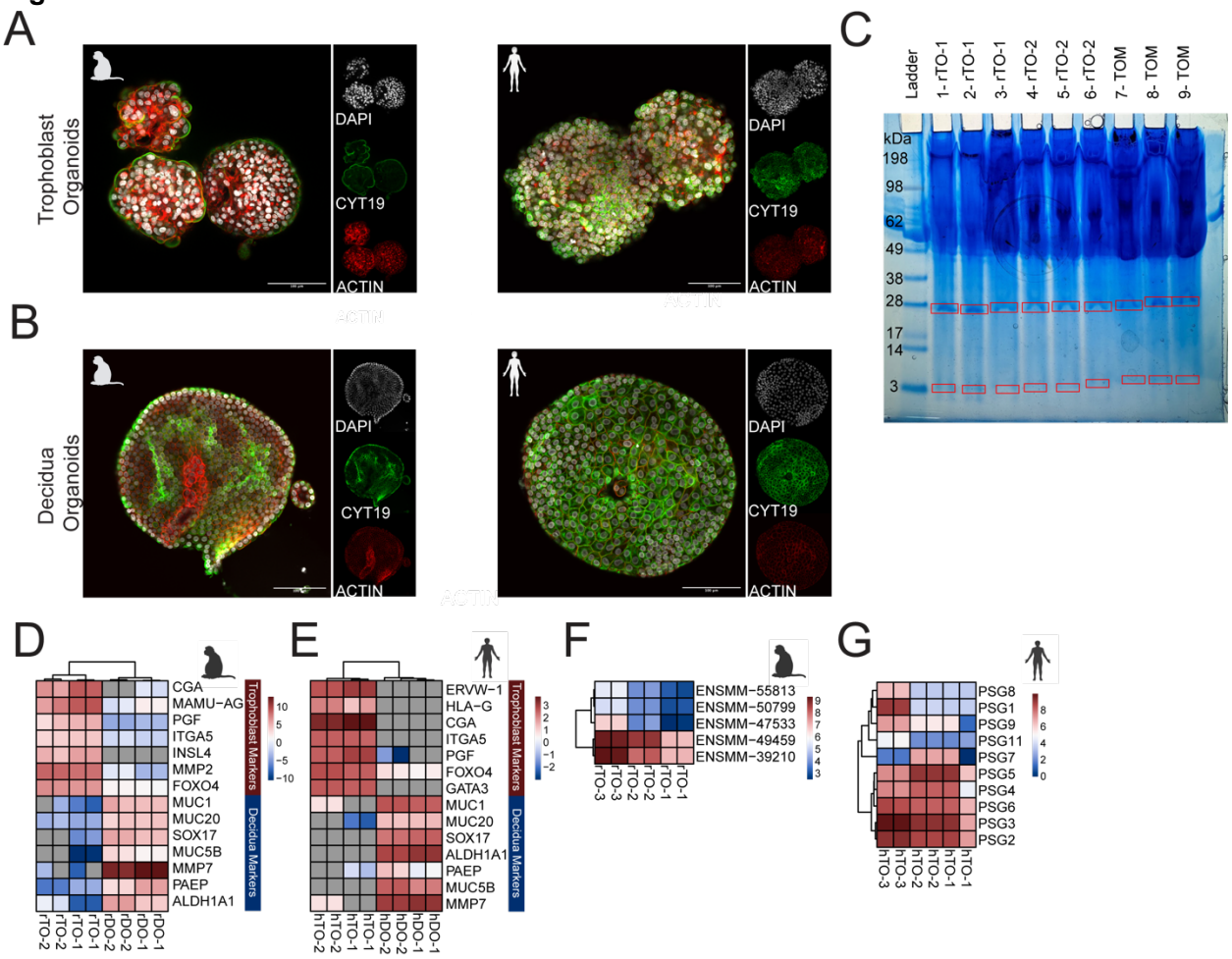


**Supplemental Figure 1. Validation of rTOs and rDOs. (A),** Confocal micrographs of rTOs and hTOs immunostained for CYT-19 (green), ACTIN (red), DAPI-stained nuclei are in black and white. Scale bar, 100μm. **(B),** Confocal micrographs of rDOs and hDOs immunostained for CYT-19 (green), ACTIN (red), DAPI-stained nuclei are in black and white. Scale bar, 100μm. **(C),** SDS-PAGE gel of rTO CM samples. Red boxes indicate bands that were excised and used for mass spectrometry. **(D),** Heatmap (based on $\log_2$ RPKM values) of transcripts expressed in rDOs and rTOs that are associated with markers of rhesus macaque trophoblasts and decidua. Data shown is 2 biological replicates and 2 technical replicates in rTOs and rDOs. **(E),** Heatmap (based on $\log_2$ RPKM values) of transcripts expressed in hDOs and hTOs that are associated with markers of human trophoblasts and decidua. Data shown is 2 biological replicates and 2 technical replicates in rTOs and rDOs. **(F),** Heatmap (based on $\log_2$ RPKM values) of identified pregnancy-specific glycoproteins (PSGs) transcripts expressed in rTOs. Data shown is 3 biological replicates and 2 technical replicates in rTOs. **(G),** Heatmap (based on $\log_2$ RPKM values) of known pregnancy-specific glycoproteins (PSGs) transcripts expressed in hTOs. Key at right. Red indicates high levels of expression, blue indicates low levels of expression, and gray indicates no reads detected. Data shown is 3 biological replicates and 2 technical replicates in hTOs.

**Figure S2**

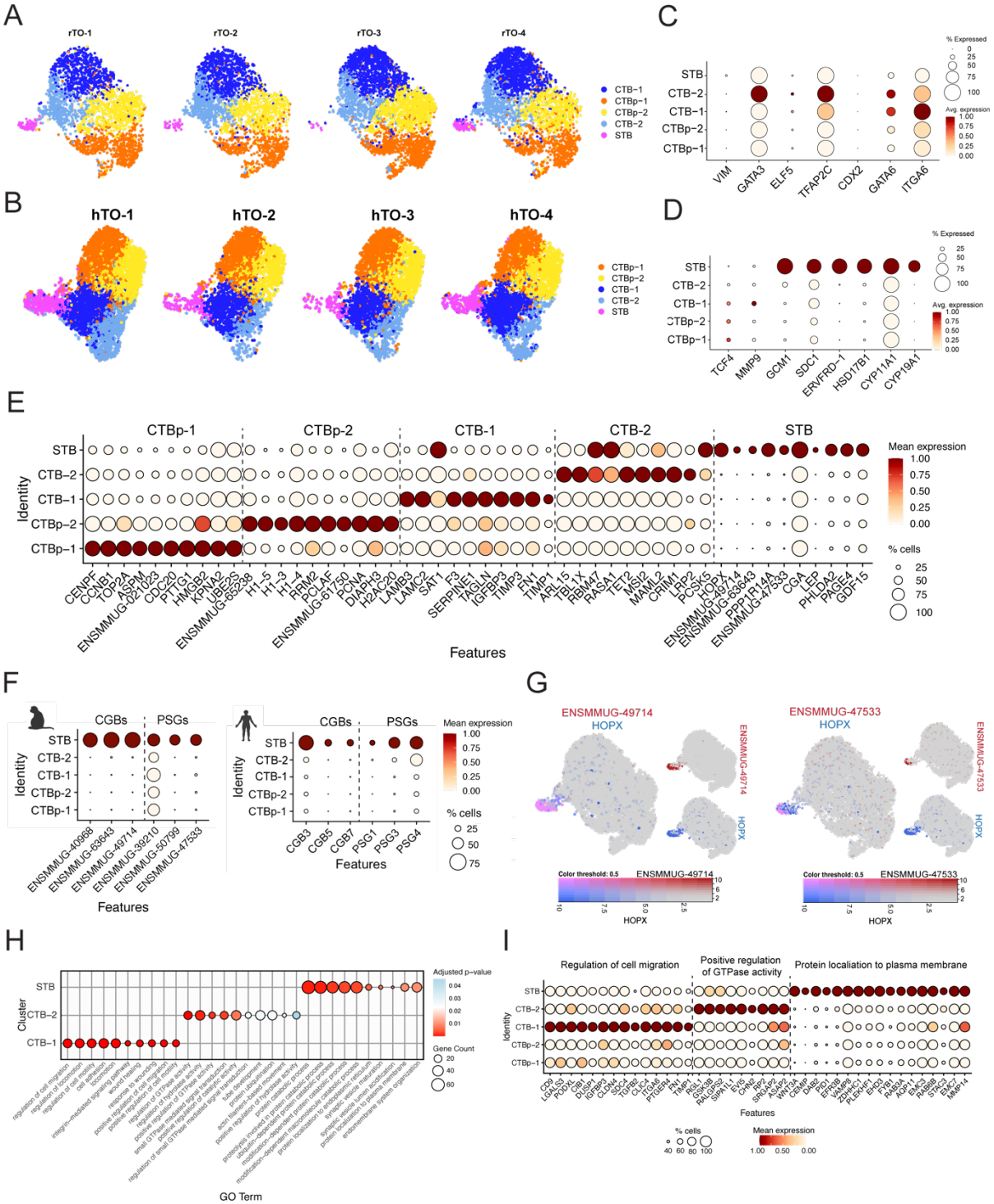


**Supplemental Figure 1. Defining cell types in rTO and hTO datasets.** Individual UMAPs from samples of **(A)** Four rTO samples and **(B)** Four hTO samples. Dotplots of gene expression of **(C)** cytotrophoblast markers and **(D)** syncytiotrophoblast or extravillous trophoblast markers in rTOs. **(E),** Dotplot of top 10 markers in each cluster in rTOs. Key at right. **(F),** Dotplot of rhesus CGBs and PSGs in rTOs (left) and human CGBs and PSGs in hTOs (right). Key at right. **(G),** Combined

feature plots of rhesus CGB (ENSMMUG00000049714) and HOPX (left) and rhesus PSG (ENSMMUG00000047533) and HOPX (right) in rTOs. Key at bottom. **(H),** Top biological processes for CTB-1, CTB-2, and STB clusters in rTOs identified using ClusterProfiler. **(I),** Dot plots of genes associated with top biological processes in CTB-1, CTB-2 and STB clusters in rTOs.

**Figure S3**

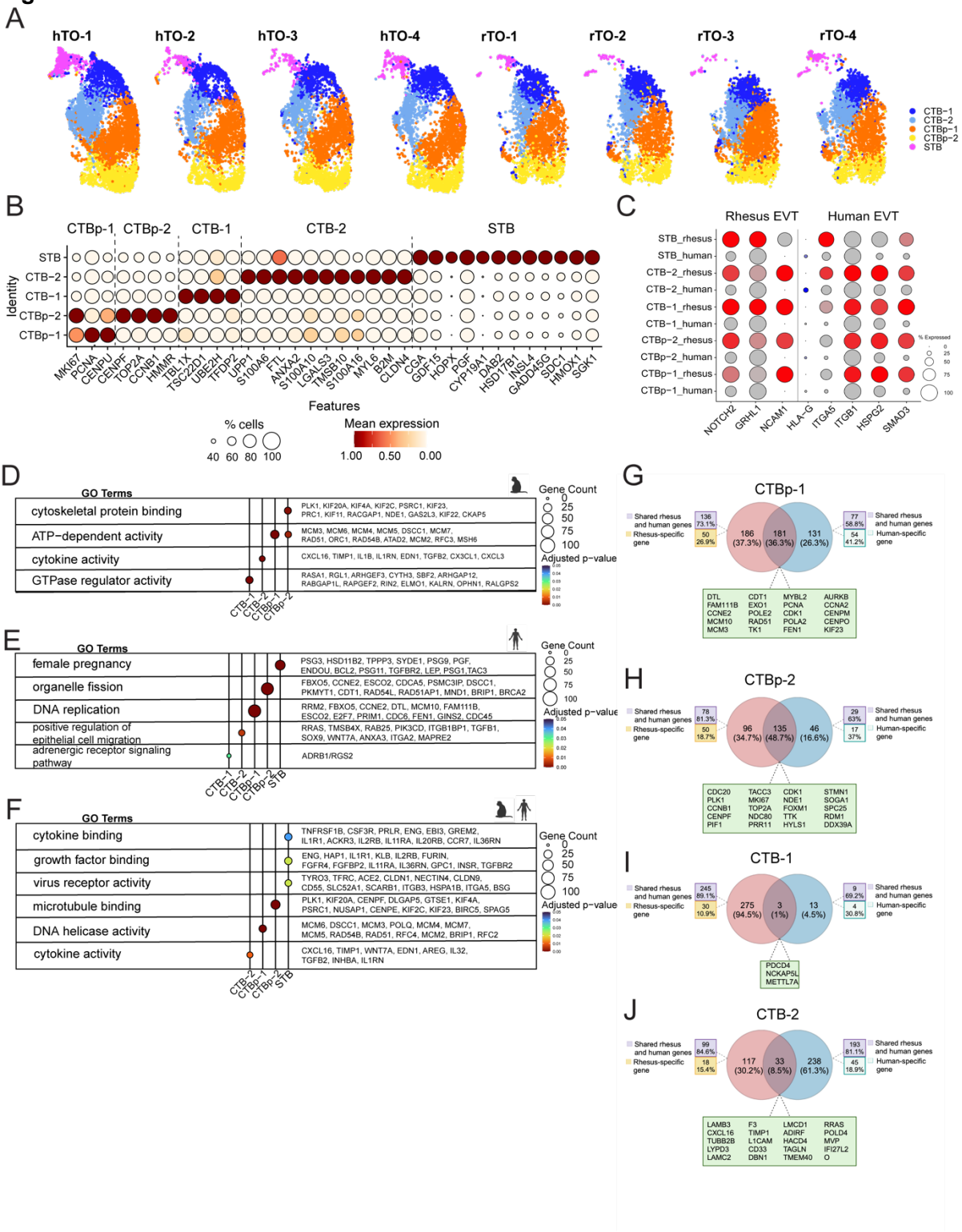


**Supplemental Figure 3. Defining cell types in integrated dataset with rTO and hTO. (A),** Individual UMAP of hTO and rTO samples that comprise that integrated dataset. **(B),** Dotplot of gene expression of cytotrophoblasts, proliferative cytotrophoblasts, and syncytiotrophoblasts. **(C),** Dotplot of rhesus macaque and human extravillous trophoblast markers in the integrated dataset

(rhesus are shown in red and human shown in blue). **(D, E, F)** Subset of pathways from GO term enrichment in all clusters in subsetted (D) rTO dataset and (E) hTO (F) integrated rTO and hTO dataset. Venn diagram of markers in the rhesus and human **(G)** CTBp-1, **(H)** CTBp-2, **(I)** CTB-1, **(J)** CTB-2 clusters that identifies shared and distinct markers. Markers that were not shared are shown as genes that are present in both the rhesus macaque and human genome as well as markers that are specific to one genome.

**Figure S4**

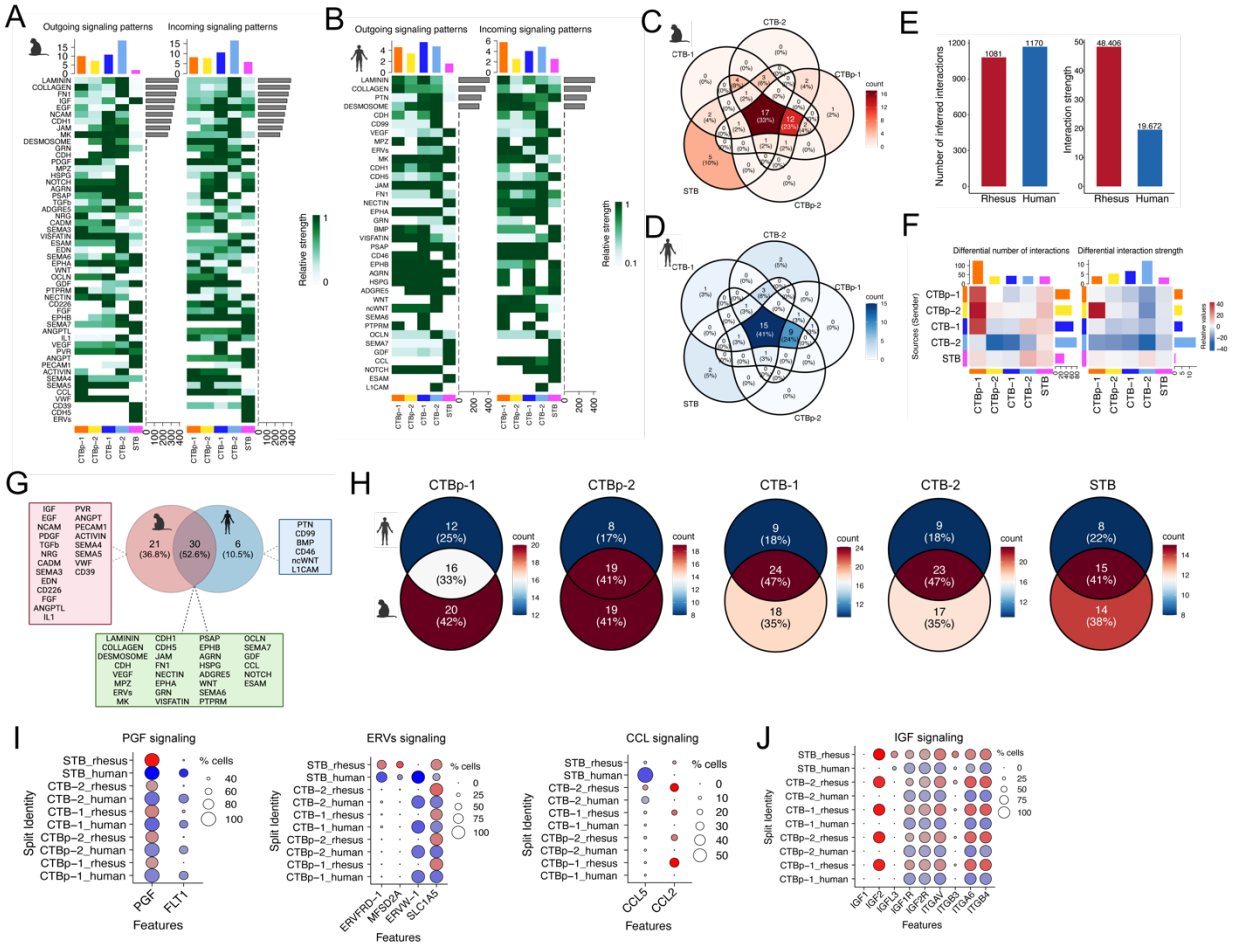


**Supplemental Figure 4. Comparative Cell Chat Analysis in rTOs and hTOs. (A, B)** Heatmap of outgoing and incoming signaling pathways based on cell cluster in rTO (A) and hTO (B). The relative signaling strength is shown by the colorbar. Overall signaling strength of signaling pathway is shown by bar plot at right. Key at right. **(C,D),** Venn diagram of signaling pathway identified in each cluster in rTOs (C) and hTOs (D). **(E),** Bar plot illustrating the number of inferred interactions in rhesus and humans (left) and their interaction strength (right). **(F),** Heatmap of number of interactions and differential interaction strength in the integrated dataset based on the cluster that sends the signal. **(G)** Venn diagram of total signaling pathways shared and different between rTOs and hTOs. **(H)** Venn diagrams depicting the number of shared, rTO-specific, and hTO-specific signaling pathways present based on cluster. **(I),** Dotplots of genes associated with PGF, ERVs, CCL and IGF signaling pathways in integrated rTO and hTO dataset separated by hTO and rTO condition. Key at right.

1253 **Supplemental Table 1. Metadata of animal study design.**

| Tissue Code | |
|---|---|
| 01 | CMV-seropositive healthy pregnancy; CD8b depleted at 55 days gestation, ~141 days gestation age- elective C-section |
| 02 | CMV-seronegative dams inoculated with FL-RhCMV + RhCMV UCD52 in early 2nd trimester and C-section near term gestation |
| 03 | |
| 04 | |
| 05 | |
| 06 | |
| 07 | CMV-seropositive healthy pregnancy; Anti-CD20 antibody administered for B Lymphocyte depletion at 53 days gestation and elective C-section at 144 days gestation |

1254

1255

1256

1257

1258

1259

1260

1261

1262

1263

1264

1265

1266

1267

1268

1269 **Supplemental Table 2.** Metadata of trophoblast organoid lines.
1270

| Experiment | TO code | Gestational age | TOs sex | TO passage number |
|---|---|---|---|---|
| Bulk RNA-seq of rTOs | rTO02 | 154d | F | P3 |
| | rCO02 | 154d | F | P3 |
| | rCO01 | 141d | F | P2 |
| Bulk RNA-seq of rDOs | rDO01 | 141d | F | P5 |
| | rDO02 | 154d | F | P2 |
| Bulk RNA-seq of hTOs | TO74 | 41w | M | P5 |
| | CO80 | 40w | F | P3 |
| | CO82 | 40w | M | P3 |
| Bulk RNA-seq of hDOs | DO77 | 40w | F | P4 |
| | DO76 | 40w | F | P5 |
| Mass Spectrometry | rCO02 | 154d | F | P3, P4, P7 |
| | rCO05 | 143d | F | P3, P6, P7 |
| Radioimmunoassay | rTO02 | 154d | F | P3, P5, P6, P7 |
| | rTO05 | 143d | F | P6, P7 |
| | rTO04 | 149d | F | P4 |
| scRNA-seq of rTOs | rCO01 | 141d | F | P3 |
| | rCO02 | 154d | F | P2 |
| | rTO02 | 154d | F | P4 |
| | rTO05 | 143d | F | P3 |
| scRNA-seq of hTOs | CO80 | 40w | F | P5 |
| | TO68 | 27w | M | P12 |
| | CO82 | 40w | M | P4 |
| | CO81 | 40w | F | P4 |

1271
1272
1273
1274
1275
1276

**Supplemental Table 3.** Components of term trophoblast organoid (tTOM) media.

| Media Components | Final Concentration |
|---|---|
| 100X N2 | 1X |
| 50X B27 | 1X |
| 500X Primocin | 100ug/mL |
| 80X N-Acetyl-L-cysteine (NAC) | 1.25mM |
| 100X L-glutamine | 2mM |
| 10000X A83-01 | 500nM |
| 10000X CHIR99021 | 1.5μM |
| 2000X Recombinant human EGF | 50ng/mL |
| 2000X Recombinant human R-spondin1 | 80ng/mL |
| 2000X Recombinant human FGF2 | 100ng/mL |
| 2000X Recombinant human HGF | 50ng/mL |
| 100X Nicotinamide | 10mM |
| 200X Y-27632 | 5μM |
| 2000X PGE2 | 2.5μM |
| FBS | 10% (vol/vol) |
| Advanced DMEM/F12 | 1X |

**Supplemental Table 4.** Components of decidua organoid media

| Media Components | Final Concentration |
|---|---|
| 100X N2 | 1X |
| 50X B27 | 1X |
| 500X Primocin | 100ug/mL |
| 80X N-Acetyl-L-cysteine (NAC) | 1.25mM |
| 100X L-glutamine | 2mM |
| 10000X A83-01 | 500nM |
| 2000X Recombinant human EGF | 50ng/mL |
| 2000X Recombinant human R-spondin1 | 80ng/mL |
| 2000X Recombinant human FGF10 | 100ng/mL |
| 2000X Recombinant human HGF | 50ng/mL |
| 1000X Recombinant human Noggin | 100 ng/mL |
| 100X Nicotinamide | 10mM |
| Advanced DMEM/F12 | 1X |

1372 **Supplemental Table 5.** Antibodies used for immunofluorescence staining.

| Antibody | Source | Catalog number | Additional Information |
|---|---|---|---|
| Mouse monoclonal Cytokeratin-19 | Abcam | ab9221 | 1:500 |
| Rabbit monoclonal Cytokeratin-19 | Abcam | ab52625 | 1:500 |
| Mouse monoclonal Mucin 5AC | Abcam | ab3649 | 1:500 |
| Rabbit polyclonal E-cadherin | Invitrogen | PA5-85088 | 1:500 |
| Rabbit monoclonal SDC-1 | Abcam | ab128936 | 1:500 |
| ITGA6 | | | |
| Alexa Fluor 594-conjugated phalloidin | Invitrogen | A12381 | 1:1000 |
| Alexa Fluor 488 Goat Anti-mouse IgG secondary antibody | Invitrogen | A32723 | Secondary antibody 1:1000 |
| Alexa Fluor 594 Goat Anti-mouse IgG secondary antibody | Invitrogen | A11032 | Secondary antibody 1:1000 |
| Alexa Fluor 594 Goat Anti-rabbit IgG secondary antibody | Invitrogen | A11037 | Secondary antibody 1:1000 |

1373
1374
1375
1376
1377
1378
1379
1380
1381
1382
1383
1384
1385
1386
1387

1388 **Supplemental Movie 1**: Three-dimensional reconstruction of a rhesus trophoblast organoid
1389 immunostained for SDC-1 (in green) and cytokeratin-19 (in red). DAPI-stained nuclei are shown
1390 in blue.
1391 **Supplemental Movie 2**: Three-dimensional reconstruction of a rhesus decidua organoid
1392 immunostained for cytokeratin-19 (in green) and E-cadherin (in red). DAPI-stained nuclei are
1393 shown in blue.
1394
1395